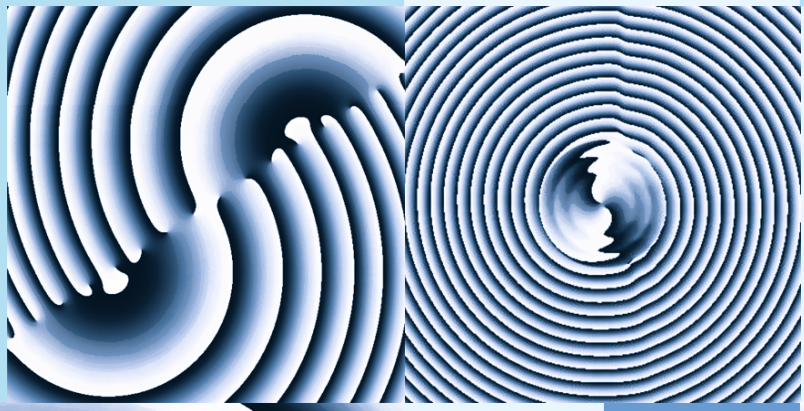
Journal of Biomedical Photonics & Engineering

Volume 7, issue 3

Special Issue

VII International Conference on Information Technology and Nanotechnology (ITNT-2021)







Special Issue Editors:
Ivan A. Bratchenko and
Victor V. Kotlyar

© 2021 J-BPE

 doi: 10.18287/JBPE21.07.030001

Journal of Biomedical Photonics & Engineering
by Samara National Research University

Volume 7, Issue 3 (Spetember 2021)

Special Issue
"VII International Conference on Information Technology and Nanotechnology (ITNT-2021)"

Special Issue Editors

Ivan A. Bratchenko
Samara National Research University, Russia

Viktor V. Kotlyar
Image Processing Systems Institute of RAS –
Branch of the FSRC "Crystallography and Photonics" RAS, Russia

Editor-In-Chief

Valery V. Tuchin - Saratov National Research State University, Russian Federation;
Institute of Precision Mechanics and Control RAS, Russian Federation; a corr.-member of RAS

Deputy Editor-In-Chief

Valery P. Zakharov - Samara National Research University, Russian Federation

Postal address:
39B Lukacheva st., room #301
Samara 443086, Russian Federation

 © 2021 J-BPE

Contents

Articles

Application of Frequency Features of Optical Flow for Event Detection in Video-EEG Monitoring Data 030301
Dmitry Murashov, Yury Obukhov, Ivan Kershner, and Mikhail Sinkin

A Method for Assessing the Pupil Center Coordinates in Eyetracking with a Free Head Position 030302
Gennadiy I. Gromilin and Nikolay S. Yakovenko

Registration of Regeneration in Planarians from Photographic Images 030303
Kharlampiy Tiras, Leonid Mestetsky, Svetlana Nefedova, and Nikita Lomov

Numerical Modeling of Radiation Focusing by Dielectric Microcylinders with Several Layers 030304
Alexandra A. Savelyeva and Elena S. Kozlova

Hyperspectral Camera – Attachment for Microscopy 030305
Mohammed M. Hamza, Ali Hamandi, Andrey R. Makarov, Vladimir V. Podlipnov, and Roman V. Skidanov

Characterization of Polarization Holographic Gratings Obtained on Azopolymer Thin Films by Digital Holographic Microscopy 030306
Veronica Cazac, Constantin Loshmanschii, Elena Achimova, Alexei Meshalkin, Vladimir Abashkin, and Vladimir Podlipnov

 © 2021 J-BPE

Application of Frequency Features of Optical Flow for Event Detection in Video-EEG Monitoring Data

Dmitry Murashov[1*], Yury Obukhov[2], Ivan Kershner[2], and Mikhail Sinkin[3,4]

[1] Federal Research Center "Computer Science and Control" of RAS, 44 Vavilova str., Moscow 119333, Russia
[2] Kotel'nikov Institute of Radio Engineering and Electronics of RAS, 11 Mokhovaya str., Moscow 125009, Russia
[3] N. V. Sklifosovsky Research Institute for Emergency Medicine of Moscow Healthcare Department, 3 Bolshaya Sukharevskaya Square, Moscow 129090, Russia
[4] A. I. Yevdokimov Moscow State University of Medicine and Dentistry, 9A Vucheticha str., Moscow 127473, Russia

*** e-mail:** d_murashov@mail.ru

Abstract. The work is devoted to the study of the frequency features of the optical flow obtained from the video record of long-term video-electroencephalographic (video-EEG) monitoring data of patients with epilepsy. It is necessary to obtain features to recognize epileptic seizures and differentiate them from non-epileptic events. We propose to analyze the periodograms of the smoothed optical flow computed from the fragments of the patient's video recordings. We use Welch's method to obtain periodograms. The values of the power spectral density of the optical flow at the selected frequencies are used as features. Using the clustering algorithm, seven groups of events are identified in video recordings and combined into three generalized classes. We train SVM classifier and conduct recognition of events in a test sample of 103 video fragments in four patients. The experiment indicates the accuracy of event classification equal to 90.3%. © 2021 Journal of Biomedical Photonics & Engineering.

Keywords: video-electroencephalographic monitoring; optical flow; periodogram; Welch's method; clustering; classification.

Paper #3432 received 25 May 2021; revised manuscript received 12 Jul 2021; accepted for publication 14 Jul 2021; published online 30 Sep 2021. doi: 10.18287/JBPE21.07.030301.

1 Introduction

In clinical practice, video-electroencephalographic monitoring, a method of long-term synchronous recording of an electroencephalogram (EEG) and video image, has become widely used. Simultaneous video recording of the patient's clinical state and the bioelectrical activity of the brain makes it possible to reliably diagnose epileptic seizures and differentiate them from non-epileptic events [1, 2]. For recording and visual analysis of video-EEG data, physicians use specialized software (for example, Galileo NT Line package), which has a set of functions for signal processing and analysis, as well as statistical data analysis. If diagnostically important fragments of the EEG are found, the physician needs to revise the area of interest in the video recording for visual assessment and differentiation of an epileptic and artifact event. Visual analysis of video data is extremely laborious [21]; therefore, it becomes necessary to develop methods for automatic registration of epileptic seizures from video sequences obtained during video-EEG monitoring.

Some works on the analysis of video recordings for the detection and recognition of epileptic events are known. The work [3] presents methods for measuring the motion strength and motor activity of newborns using video recording. The quantitative characteristics obtained in the form of signals are used to differentiate myoclonic and clonic seizures and to distinguish seizures from the normal behavior of the newborn. The motion strength is defined as the area of the moving parts of the infant's body. To outline such fragments, the wavelet transform of frames, median filtering, and segmentation operations using an adaptive version of the k-means algorithm are used. The change in time of the coordinates of characteristic points, selected automatically on the child's limbs and tracked using the KLT (Kanade-Lucas-Tomasi) algorithm, generates signals that characterize

motor activity. Modifications of methods for measuring motion strength and motor activity are presented in the works [4, 5].

In the works [6, 7], the authors solved the problem of real-time detection of clonic seizures in newborns by the sequence of images obtained from video cameras. The value of the filtered average optical flow calculated as the sum of the binarized pixel-by-pixel difference in luminance of adjacent frames of the video sequence is analyzed. In Ref. [6], a feature of a seizure is the periodicity of the optical flow, which is detected using a hybrid autocorrelation-YIN estimation technique. In Ref. [7], the Maximum Likelihood criterion is used to determine the periodicity of the optical flow.

The paper [8] presents an algorithm for recognizing convulsive seizures in real-time from a sequence of frames recorded by a video camera. To analyze video images and detect events, the method described in Ref. [9] is used. The method consists in computing the components of the optical flow associated with group transformations of objects in frames (translation, rotation, dilatation, shear) and band-pass temporal filtering to identify an occurrence of clonic movements.

In the works [10, 11], the authors analyze video sequences recorded by multiple cameras to detect nocturnal motor seizures and central apneas occurring in the aftermath of epileptic seizures. The characteristics of the sigmoid patterns of the time-frequency spectrum (modulation maximum amplitude and total spectral power modulation at the time of the event) in the range of 0.1–1 Hz of translation, dilatation, and shear rates are used as features of a diagnostic event. These velocities are calculated by the method described in Ref. [9] from the optical flow generated by the patient's movements.

Previously, the authors of studies [12, 13] proposed to detect events in a video recording by the magnitude of the optical flow, which characterizes the degree of mobility of the frame area in which the patient is located. The algorithm was designed to detect both convulsive and non-convulsive seizures. The tests showed that the detected events quite accurately coincided with the events detected during the analysis of the EEG wavelet spectrograms. In Ref. [14], an algorithm for the synchronous analysis of the EEG signal and video recording for the detection and differentiation of diagnostic and artifact events was proposed. The algorithm combines a threshold detector of brain activity using the ridges of wavelet spectrograms [15] and a threshold detector of events in terms of optical flow [12, 13]. The results of the analysis of clinical data recorded on EBNeuro equipment and Galileo NT Line package software showed the fundamental possibility of reliable distinguishing artifact events from epileptic seizures [14]. However, for more reliable recognition of epileptic seizures, additional features are needed.

The study of publications has shown that frequency analysis of signals obtained from an optical flow is widely used to extract features of epileptic seizures. This work aims to study the frequency features of the optical flow of video recording for the recognition of diagnostic and artifact events during the synchronous analysis of video-EEG data. Unlike the well-known works, the proposed technique is not restricted to a specific seizure type, and this study will consider a wider range of events recorded on video. We propose to analyze the periodograms of the smoothed optical flow, computed from the fragments of the video recording of the patients. Since this work does not consider the multidirectional components of the optical flow, the classical method of spectral analysis of signals will be used to obtain periodograms. As features, we will use the values of the power spectral density (PSD) at the selected frequencies.

2 Materials and Methods

As mentioned above, this work aims to obtain and study the features for recognizing epileptic seizures in the data of long-term video-EEG monitoring and their differentiation with non-epileptic events. In this study, we used video recordings from long-term video EEG monitoring data of seven adult patients with an active level of wakefulness. The recordings were obtained with an HD camera using the Galileo NT Line package. The camera is fixed to the ceiling of the hospital room. The duration of the recordings is from 5 to 24 h or more. Each video consists of files in AVI format containing a fragment of three minutes in length.

We will recognize events based on the analysis of the patient's movement recorded by a video camera. To measure the intensity of the patient's movement, we use the value of the smoothed total optical flow calculated in the region of interest in each frame of the video sequence. The optical flow is computed by the Lucas-Kanade method. To smooth the activity measure, we use a discrete version of the Kalman-Bucy filtering algorithm.

We form the feature descriptions of events recorded on video based on the frequency analysis of the smoothed measure of patient's activity. To compute periodograms, we use Welch's method with a Hamming window of three sizes. We propose to use the values of the power spectral density of a measure of the patient's mobility at 14 selected frequencies as the features of events. To analyze the obtained feature descriptions of events and study the possibility of using pattern recognition algorithms for detecting events, we use a clustering algorithm with automatic choosing the optimal number of clusters. We use the Support Vector Machine (SVM) classifier to recognize events in video recordings. The classifier was trained on 78 three-minute video fragments of three adult patients with an active level of wakefulness. For testing, we used 103 video fragments of the other four adult patients.

In the following sections of the article, we describe in detail the application of the listed above methods and data in our research.

2.1 A measure of patient's activity

Analysis of publications in the domain of detecting seizures from video sequences showed that the most

common approach is based on the analysis of optical flow. In works [13, 14] we proposed to detect diagnostic events using the measure, characterizing the degree of activity of the region of interest. The region of interest is the part of the frame where the patient is located. A measure of the activity of the region of interest is the total value of the optical flow calculated for each frame of the video sequence:

$$J(n) = \frac{1}{WH}\sum_{x=0}^{W-1}\sum_{y=0}^{H-1}\sqrt{V_x^2(x,y,n) + V_y^2(x,y,n)} + \delta(n), \quad (1)$$

where $J(n)$ is the value of activity measure calculated in the frame number n; W is the width and H is the height of the region of interest in pixels; $V_x(x,y,n)$, $V_y(x,y,n)$ are the optical flow values in axial directions X and Y in the frame number n at a pixel with coordinates (x,y); $\delta(n)$ is noise. The measure of activity J characterizes the intensity of movement of objects (patients) in the region of interest in frames of a video recording. To compute $V_x(x,y,n)$ and $V_y(x,y,n)$ in Eq. (1), we applied the Lucas–Kanade algorithm [16]. Two examples of seizure and food intake events from video-EEG data of two patients and computed optical flow vector fields are shown in Fig. 1 (a) and (b).



(a)



(b)

Fig. 1 Frames fixing seizure (a) and food intake (b) events from video-EEG data of two patients and computed optical flow vector fields (shown as arrows). The size of the shown region of interest is 800 by 570 pixels, and the size of the corresponding field of view is about 120 by 90 cm.

As far as the noise component is present in model (1), we use the smoothed value of the activity measure $\hat{J}(n)$ to detect events. The smoothed $\hat{J}(n)$ value is obtained using a discrete version of the Kalman-Bucy filtering algorithm [17]. We apply the Kalman-Bucy algorithm because it provides the optimal estimate in the sense of minimum error variance. The graphs of the values of measure of activity $J(n)$ and smoothed measure of activity $\hat{J}(n)$ obtained from a real video recording are shown in Fig. 2. In this video from 126 to 180 sec, an epileptic seizure is captured. The decision to fix a diagnostic event is made according to the threshold rule. To increase the reliability of event detection, it is necessary to take into account not only the amplitude but also the frequency characteristics of the measure of activity. In the next subsection, we will present a technique for extracting the frequency features of the smoothed measure of patient's activity $\hat{J}(n)$.

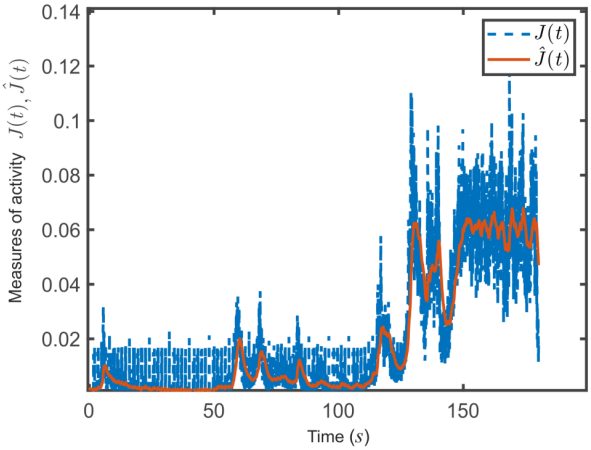


Fig. 2 Graphs of measure of activity J and smoothed measure of patient's activity $\hat{J}$ obtained from a video recording of an epileptic seizure. The measure of activity J (as well as the smoothed measure $\hat{J}$) characterizes the intensity of movement of patients in the region of interest in frames of a video recording.

2.2 Extracting frequency features of events

To construct periodograms, we use the Welch method with a Hamming window with 50% overlap [18]. The analyzed video data are presented in the form of three-minute fragments of the patient's video recording which fix various events and their combinations: seizures, sleep, movement, food intake. The frame (sample) rate is equal to 20 frames per second. The sequence of samples of the value of the smoothed activity measure $\hat{J}(0), \ldots, \hat{J}(n) \ldots, \hat{J}(N-1)$ with an interval of $T = 0.05$ sec is divided into P segments of D samples in each with a shift of $S, S \le D$ samples between adjacent segments. The estimate of the Welch's periodogram in the frequency range $-\frac{1}{2T} \le f \le \frac{1}{2T}$ is determined by the following expression:

$$\hat{P}_w = \frac{1}{P}\sum_{p=0}^{P-1}\tilde{P}_{\hat{J}\hat{J}}^{(p)}(f), \quad (2)$$

where $\tilde{P}_{\hat{\jmath}\hat{\jmath}}^{(p)}$ is the spectrum of the weighted segment p,

$$\tilde{P}_{\hat{\jmath}\hat{\jmath}}^{(p)} = \frac{1}{UDT}\left|X^{(p)}(f)\right|^2, \quad (3)$$

where $X^{(p)}(f)$ is the discrete-time transformation of the segment p; U is the energy of the window w.

Using formulas (2) and (3), we obtained periodograms of different frequency resolutions at three window sizes: 10, 200, and 600 samples. Fig. 3 shows the examples of periodograms computed at window size equal to 200 from video records of different events in one of the patients. We studied 78 fragments of video recordings of three patients that fixed the following events: epileptic seizure, intense movement in the frame, sleep, rest, smooth movement, food intake. Fig. 3 shows that different events take different values of the power spectral density at a particular frequency value. To study the structure of the data that contain the obtained spectral characteristics of the optical flow, we use the technique of cluster analysis. The application of the clustering algorithm to distinguish groups of events by levels of power spectral density of periodograms obtained from video recordings of different events is described in the next subsection.

2.3 Partitioning frequency feature space

To study the possibility of using classifiers for detecting events, we applied a clustering algorithm. The algorithm is based on the search for locally optimal data partitions with automatic selection of the optimal number of clusters [19]. For optimization, the criterion for the minimum of the sum of intraclass variances is used:

$$J^{LO} = \sum_{m=1}^{k} J_m^G, \qquad J_m^G = \frac{1}{|G_m|}\sum_{\mathbf{x}_i \in G_m} \rho(\mathbf{x}_i, \mathbf{x}_m^c)^2, \quad (4)$$

where $\mathbf{x}_m^c$ is the center of group G_m, to which the object $\mathbf{x}_i$ is assigned; $\rho(\mathbf{x}_i, \mathbf{x}_m^c)$ is the distance from object $\mathbf{x}_i \in G_m$ to the center of group $\mathbf{x}_m^c$; J_m^G is the intraclass variance. Here, $\mathbf{x}_i \in R^N$, $\mathbf{x}_m^c \in R^N$, where N is the dimension of the feature space.

The optimal number of clusters k in the range $a-1 \le k \le b+1$ is determined from the condition for the maximum of the functional

$$g = \frac{l_k}{r_k}, \quad (5)$$

$$l_k = \sum_{i=a}^{k-1} \frac{\Delta_i}{2^{k-i}} + \frac{\Delta_{a-1}}{2^{k-a}}; \qquad r_k = \sum_{i=k}^{b-1} \frac{\Delta_i}{2^{i-k+1}} + \frac{\Delta_b}{2^{b-k}}, \quad (6)$$

where $\Delta_i = J_{i+1}^{LO} - J_i^{LO}$.

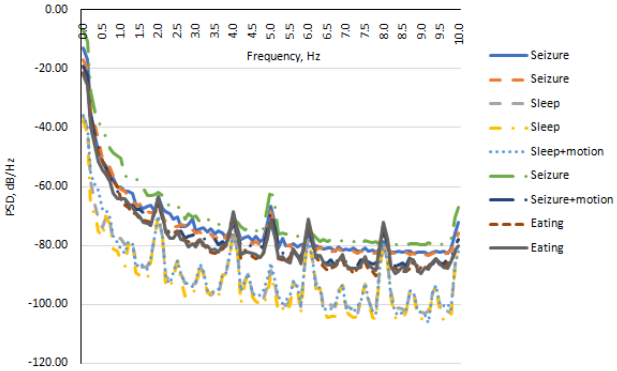


Fig. 3 Optical flow periodograms of recordings of various events for one of the patients computed at window size $D = 200$.

Table 1 Relative distances between cluster centers. Distances between the closest cluster centers are shown in bold.

Events	No	1	2	3	4	5	6	7
Eating	1	0	0.43	**0.21**	0.64	**0.17**	0.55	0.46
Seizure	2		0	0.55	1.0	0.55	0.95	**0.19**
Smooth movement	3			0	0.46	**0.11**	0.49	0.53
Sleep+movement	4				0	0.49	**0.42**	0.96
Rest after seizure	5					0	0.44	0.55
Sleep	6						0	0.98
Movement	7							0

In the study, we used a set of feature descriptions of 78 fragments of video recordings of events taken from the data of 24-h video-EEG monitoring of three adult patients with an active level of wakefulness. The feature space is formed from the PSD values of the periodograms of the optical flow obtained with three window sizes (see Section 3). The PSD values were taken at 14 frequencies selected in the range from 0.5 to 8.8 Hz. Thus, the dimension of the composited feature vectors is equal to 42. The optimal number of clusters was chosen in the range from 2 to 8.

The clustering algorithm described by formulas (4) – (6) partitioned the data extracted from the periodograms into seven groups of events characterized by similar PSD values at the selected frequencies: (1) food intake and combination of food intake and movement ("Eating"); (2) epileptical seizures ("Seizure"); (3) smooth movement ("Smooth movement"); (4) sleep and smooth movement ("Sleep + movement"); (5) rest and smooth movement after seizure ("Rest after seizure"); (6) sleep ("Sleep"), and (7) intensive movement ("Movement").

Table 1 gives the relative distances between the centers of the obtained clusters.

The results given in Table 1 show that the clusters of feature descriptions of several types of events are well-separated in the feature space, and the centers of several clusters are located relatively close. For example, the centers of the clusters "Seizure" and "Sleep", "Smooth movement" and "Movement" are significantly distant, while the centers of the clusters "Smooth movement" and "Rest after seizure", "Eating" and "Rest after seizure", as well as "Seizure" and "Movement" are located relatively close, since the nature of the patient's movements in these groups of events may be similar. Therefore, we combined closely spaced clusters and formed the following three generalized classes. The first class, "Seizure/Movement", includes epileptic seizures and episodes of intense movement in the region of interest (clusters of events "Seizure" and "Movement"). The second class, "Sleep", includes the patient's sleep and state of rest (clusters of events "Sleep" and "Sleep + movement"). The third class, "Smooth movement", includes events associated with the movements of low intensity. This class combines episodes of eating, smooth posture changes, and working with a smartphone or laptop ("Eating", "Smooth movement", and "Rest after seizure" event clusters). Thus, the frequency features extracted from the video recordings of long-term monitoring of patients made it possible to distinguish three types of patterns that characterize generalized classes of events.

In the next section, to confirm the possibility of detecting events using frequency features, we will train the SVM classifier and recognize events from the test set of fragments from long-term video recordings of patients with epilepsy.

3 Results

We used the SVM algorithm [20] to classify events. A set of 78 feature descriptions of video recordings of events, described in Section 4, was used to train the classifier. Events are grouped into three generalized classes. In the SVM algorithm, we used a potential function in the form of a dot product. The leave-one-out cross-validation procedure was used for training. The results of training and quality measure values are given in Table 2.

Feature descriptions of 103 three-min fragments of video recordings of long-term monitoring in four patients formed the test sample. The analyzed video fragments captured events given in Table 1 and their combinations, including seven seizures and five events of food intake. It should be noted that one event could be recorded in several consecutive three-minute video fragments. Table 3 presents the results of testing and values of recognition quality measures.

4 Discussion

The relatively low percentage of correctly recognized events from the "Seizure/Movement" class can be explained in the following way. The camera recorded most of the epileptic seizures from the test sample on several consecutive 3-min videos. Some records contain only the initial or final seizure stages. The duration of these stages is significantly shorter than three minutes. The size of the window used in calculating the estimates of periodograms by formulas (2), (3) is much less than the number of frames in a three-minute video

Table 2 Results of training SVM classifier.

Classes	Classified objects	True	False	From class 1	From class 2	From class 3
Seizure/Movement	21	19	2	19	0	2
Sleep	31	29	2	0	29	2
Smooth movement	25	20	5	3	2	20
Reject	1			0	0	1
Total	78 (100%)	68 (87.2%)	9 (11.2%)	22	31	25
Precision	6			90.5%	93.5%	80%
Recall	7			86.4%	93.5%	80%

Table 3 Results of recognition of a test sample.

Classes	Classified objects	True	False	From class1	From class 2	From class 3
Seizure/Movement	18	18	0	18	0	0
Sleep	26	24	2	1	24	1
Smooth movement	59	51	8	6	2	51
Total	103 (100%)	93 (90.3%)	10 (9.7%)	25	26	52
Precision				100%	92.3%	86.4%
Recall				72%	92.3%	98%
Specificity				100%	77%	84%
Negative predictive value				92%	97%	98%
F1-score				83.7%	92.3%	91.8%

Table 4 Performance of various event detection algorithms [6–11].

Algorithm/reference	Task	Precision	Recall (sensitivity)	Specificity	Negative predictive value
Kouamou Ntonfo et al. (2012) [6]	Detection of neonatal clonic seizures	27–64%	60–93%	67–86%	93–96%
Cattani et al. (2017) [7]	Apneas detection Clonic seizure detection		90–100% 76–92%	78–83% 88–96%	
Geertsema et al. (2018) [8]	Recognition of convulsive seizures		57–100%		
Kalitzin et al. (2012) [9]	Segmentation of clonic seizures		95%		
Geertsema et al. (2020) [10]	Detection of central apneas		>90%	>99%	
van Westrhenen et al. (2020) [11]	Detection of nocturnal motor seizures in children		94%		

recording, and the spectra of weighted segments (3) can vary significantly. In this case, the frequency pattern of the three-minute fragment, characterized by the estimate (2), may be deformed and assigned to the non-proper class. It should be noted that in the considered test set of video recordings, all epileptic seizures captured in several consecutive three-minute fragments are detected correctly in at least one of the fragments. In general, the percentage of correctly classified events is equal to 90.3% of the total.

Table 4 shows the characteristics of event recognition obtained by analyzing video sequences of video-EEG monitoring data by different methods presented in the works that we considered in Section 1. From the data in Tables 3 and 4 and taking into account the above remarks, it follows that the results of event detection (precision, recall, and specificity) obtained in this work correspond to the performance of the algorithms proposed in Refs. [6–11].

It is possible to increase the accuracy of event classification by reducing the duration of the analyzed video fragments and augmenting the training sample of events. Differentiation of seizures and artifacts of chewing and movement will be carried out in the synchronous analysis of video and EEG recordings.

5 Conclusions

We studied the possibility of using the frequency characteristics of the video recordings for analyzing long-term video-electroencephalographic monitoring data. Periodograms of the smoothed optical flow, calculated from the fragments of video recordings, which captured various events, were computed. To obtain periodograms, we used Welch's method with the Hamming window of three sizes. The values of the spectral power density of the optical flow at fourteen selected frequencies are used as features of events. We applied the clustering algorithm with automatic selection of the optimal number of clusters to obtain optimal data partition. The preliminary results of the frequency analysis of the optical flow, computed from the video-EEG monitoring data of patients, were obtained. Seven groups of events were identified in the feature space using the clustering algorithm. These groups were combined into three generalized classes. To confirm the possibility of detecting events by frequency

characteristics of video recordings, we trained an SVM classifier and conducted recognition of events in a test sample of 103 video fragments in four patients. The percentage of correctly classified events is equal to 90.3% of the total. Further research will be aimed at improving the accuracy of detecting events in video recordings of patients by frequency features and developing an algorithm for synchronous analysis of video-EEG monitoring data.

Disclosures

All authors declare that there is no conflict of interests in this paper.

Acknowledgements

This research was carried out within the framework of the state task and was partially supported by the RFBR, grant No 18-29-02035.

References

1. M. Patel, P.Satishchandra, J. Saini, R. D. Bharath, and S. Sinha, "Eating epilepsy: Phenotype, MRI, SPECT and video-EEG observations," Epilepsy Research 107(1–2), 115–120 (2013).
2. T. Chen, Y. Si, D. Chen, L. Zhu, D. Xu, S. Chen, D. Zhou, and L. Liu, "The value of 24-hour video-EEG in evaluating recurrence risk following a first unprovoked seizure: A prospective study," Seizure 40, 46–51 (2016).
3. N. B. Karayiannis, S. Srinivasan, R. Bhattacharya, M. S. Wise, J. D. Frost, and E. M. Mizrahi, "Extraction of motion strength and motor activity signals from video recordings of neonatal seizures," IEEE Transactions on Medical Imaging 20(9), 965–980 (2001).
4. N. B. Karayiannis, G. Tao, "Improving the extraction of temporal motion strength signals from video recordings of neonatal seizures," In Proceedings of the IEEE Conference on Advanced Video and Signal Based Surveillance, 22 July 2003, Miami, FL, USA, 87–92 (2003).
5. N. B. Karayiannis, A. Sami, J .D. Frost, M. S. Wise, and E. M. Mizrahi, "Automated extraction of temporal motor activity signals from video recordings of neonatal seizures based on adaptive block matching," IEEE Transactions on Biomedical Engineering 52(4), 676–686 (2005).
6. G. M. Kouamou Ntonfo, G. Ferrari, R. Raheli, and F. Pisani, "Low-Complexity Image Processing for Real-Time Detection of Neonatal Clonic Seizures," IEEE Transactions on Information Technology in Biomedicine 16(3), 375–382 (2012).
7. L. Cattani, D. Alinovi, G. Ferrari, R. Raheli, E. Pavlidis, C. Spagnoli, and F. Pisani, "Monitoring infants by automatic video processing: A unified approach to motion analysis," Computers in Biology and Medicine 80, 158–165 (2017).
8. E. E. Geertsema, R. D. Thijs, T. Gutter, B. Vledder, J. B. Arends, F. S. Leijten, G. H. Visser, and S. N. Kalitzin, "Automated video-based detection of nocturnal convulsive seizures in a residential care setting," Epilepsia 59(S1), 53–60 (2018).
9. S. Kalitzin, G. Petkov, D. Velis, B. Vledder, and F. L. da Silva, "Automatic Segmentation of Episodes Containing Epileptic Clonic Seizures in Video Sequences," IEEE Transactions on Biomedical Engineering 59(12), 3379–3385 (2012).
10. E. E. Geertsema, G. H. Visser, J. W. Sander, and S. N. Kalitzin, "Automated non-contact detection of central apneas using video," Biomedical Signal Processing and Control 55, 101658 (2020).
11. A. van Westrhenen, G. Petkov, S. N. Kalitzin, R. H. C. Lazeron, and R. D. Thijs, "Automated video-based detection of nocturnal motor seizures in children," Epilepsia 61(S1), S36–S40 (2020).
12. D. Murashov, Yu. Obukhov, I. Kershner, and M. Sinkin, "Detecting Events in Video Sequence Of Video-EEG Monitoring," International Archives of the Photogrammetry, Remote Sensing and Spatial Information Sciences 42(2/W12), 155-159 (2019).
13. D. Murashov, Yu. Obukhov, I. Kershner, and M. Sinkin, "A technique for detecting diagnostic events in video channel of synchronous video and electroencephalographic monitoring data," CEUR Workshop Proceedings 2391, 285–292 (2019).
14. D. M. Murashov, Y. V. Obukhov, I. A. Kershner, and M. V. Sinkin, "An algorithm for detecting events in video EEG monitoring data of patients with craniocerebral injuries," Computer Optics 45(2), 301-305 (2021).
15. K. Obukhov, I. Kersher, I. Komoltsev, and Yu. Obukhov, "Epileptiform Activity Detection and Classification Algorithms of Rats with Post-traumatic Epilepsy," Pattern Recognition and Image Analysis 28(2), 346-353 (2018).
16. B. D. Lucas, T. Kanade, "An iterative image registration technique with an application to stereo vision," Proceedings of Imaging Understanding Workshop, 121-130 (1981).
17. R. E. Kalman, R. S. Bucy, "New results in linear filtering and prediction theory," Journal of basic engineering 83(1), 95-108 (1961).
18. S. L. Jr. Marple , Digital spectral analysis with applications, Prentice-Hall, Inc., Englewood Cliffs, NJ (1987).
19. Yu. I. Zhuravlev, V. V. Ryazanov, and O. V. Sen'ko, Recognition, Mathematical methods. Software system. Practical applications, Phasis, Moscow (2006) [In Russian].

20. R. O. Duda, P. E. Hart, and D. Stork, Pattern classification, 2nd ed., A Wiley-Interscience Publication, New York (2001).
21. J. Dobesberger, G. Walser, I. Unterberger, K. Seppi, G. Kuchukhidze, J. Larch, G. Bauer, T. Bodner, T. Falkenstetter, M. Ortler, G. Luef, and E. Trinka, "Video-EEG monitoring: safety and adverse events in 507 consecutive patients," Epilepsia 52(3), 443-52 (2011).

A Method for Assessing the Pupil Center Coordinates in Eyetracking with a Free Head Position

Gennadiy I. Gromilin* and Nikolay S. Yakovenko
Institute of Automation and Electrometry SB RAS, 1 Academician Koptyug Ave., Novosibirsk 630090, Russia

*** e-mail:** gromilin@iae.nsk.su

Abstract. IR-illuminated Eyetracking systems include cornea reflection and pupil center coordinates detection to calculate the operator's gaze fixation point. When you turn a view of a large angle, some of the frames are blurred, and the coordinates are unreliable. The article describes a method for determining the center of the pupil in the gaze fixation system for operation at an increased camera frame rate. Comparison with known algorithms is given. The algorithm execution average time is about 1.2 ms on a typical office computer by processing images in fragments of the order of 340x240 pixels. © 2021 Journal of Biomedical Photonics & Engineering.

Keywords: Eyetracking system; cornea reflection; pupil center; aiming point, view direction.

Paper #3431 received 25 May 2021; revised manuscript received 6 Sep 2021; accepted for publication 6 Sep 2021; published online 30 Sep 2021. doi: 10.18287/JBPE21.07.030302.

1 Introduction

Person's gaze determining systems are beginning to be applied in various areas of activity. In technology – the devices control, first, remotely unmanned devices [1, 2]. In medicine, it is the detection of the human condition in psychology [3], the study of the central nervous system [4], the assessment of visual acuity in ophthalmology [5]. In marketing, Eyetracking is used to study how to inspect a scene when promoting products [6]. The considered system is designed to device control.

The most widespread approaches are systems with IR illumination of the eyes, which provide the greatest contrast between the pupil and the iris and the least influence of extraneous illumination. For each video stream frame in such systems, the main algorithms are executed:

- finding eye cornea reflections from illuminators and determining their coordinates;
- finding the pupil and determining its center coordinates;
- calculation gaze points from the cornea reflection and the pupil center coordinates.

With free head position, the size of the eye area is significantly smaller than the size of the frame. To reduce the processing time, the eye area is localized first. Region of interest (ROI) selection is used when processing various types of images, for example, medical [7, 8]. In this paper, the task is simplified by presence of the cornea reflections from IR illuminators, which is brighter than the rest of the image. Cornea reflections are easy to detect, but you need to sort them into true and parasitic ones.

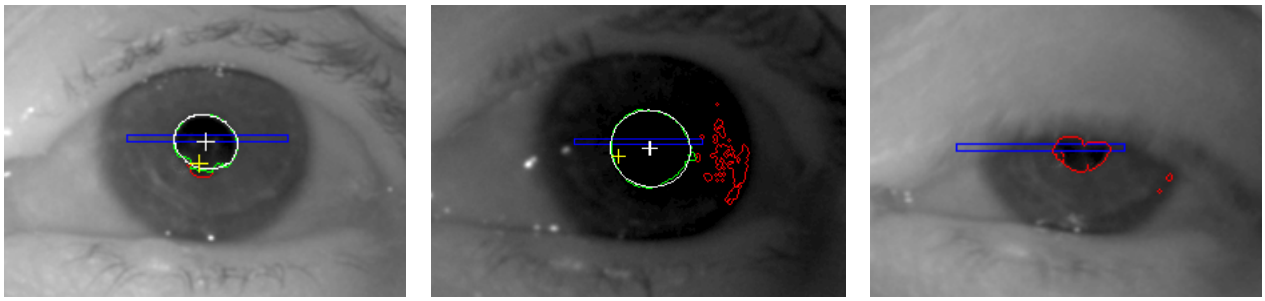
During saccades movements eye movement speed reaches 450–700 deg/sec. In Eyetracking system with a frame rate of 30–50 Hz the eye image is blurred, which prevents the necessary accuracy of the gaze direction registration.

The proposed algorithm uses threshold selection of the pupil boundary and adaptive threshold estimation, which require significantly less computational resources.

2 Materials and Methods

When the camera is not mounted on a person's head, it is necessary that the camera image capture an area approximately twice the distance between the eyes in order to track the operator head's movement. In this case, it is necessary to determine the eyes position in the image before the pupil searching.

The system uses IR LED illumination, which increases the contrast between the pupil and the iris. In addition, bright small size corneal reflections are formed on the cornea of the eye. Therefore, it is possible to allocate the fragments including the eye image, and image processing should be carried out in the fragments. To reduce the computational resources needs, the cutoff threshold carries out the pupil boundaries selection.



(a) (b) (c)

Fig. 1 Selection of the pupil boundaries: (a) a fragment with good selection, (b) elimination of unnecessary contours, (c) reduction of the area when winking. Fragment sizes are about 240×180 pixels.

While the difference in the pupil and the iris brightness is small, and the lighting conditions may be changed, an adaptive threshold is applied, which is adjusted at each frame in which the pupil is detected. Fig. 1a shows the stages of eye image processing.

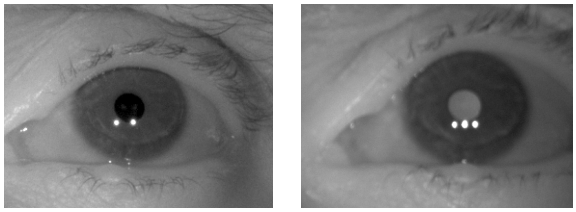
Start point for pupil search is marked with a blue cross. The threshold level is estimated inside the blue rectangle for red outlines. RANSAC (Random Sample Consensus) algorithm [9] has left a green contour, along which the white ellipse parameters were estimated.

After the detection and selection of corneal reflections (Fig. 2), the fragment with the eye image is allocated and the procedure for isolating the pupil boundaries and the ellipse parameters is performed (Fig. 1a).

To obtain the coordinates of the pupil center, the following steps are performed:

- thresholding the image;
- searching areas boundaries and selection a specified range length contour (Fig. 1b);
- selecting boundary points inliers by the RANSAC [9];
- refinement the ellipse parameters by the least squares method [10];
- estimation current frame threshold value and recursive filtering by time (frame number).

At the first pupil search, the threshold is estimating before threshold procedure. The assessment is provided on the area outlined by a blue rectangle. The area is getting out above patches of corneal reflections as IR LEDs are below the monitor. After filtration for noise reduction, the threshold level is getting out in the middle between a pupil and an iris brightness. This approach works both at dark and at light pupils (Fig. 2).



(a) (b)

Fig. 2 Fragments about 280×220 pixels of an eye images with a dark (a) and light (b) pupil.

The binary image is obtained by using the threshold. The boundary contours of the regions are found and highlighted by OpenCV findContours() method, described in the Ref. [11], and discarded the contours with boundary length outside the specified range.

The chosen contour boundary points are checked by RANSAC for belongs to the ellipse model. The parameters of the ellipse are clarified by the least square method from OpenCV fitEllipseDirect() function.

A change of the pupil area is also checked, and if the change is greater than the specified one, the frame is discarded. Fig. 1c shows the change in pupil size when winking.

After obtaining the corneal reflection and the pupil center coordinates, the three-dimensional cornea center coordinates and the gaze direction are determined. The intersection of the gaze vector with the monitor plane defines the gaze fixation point.

3 Results

Fig. 3 shows the layout diagram of the breadboard device. The camera and IR LEDs are located under the industrial monitor. Left and right side LEDs creates cornea reflections to determine the three-dimensional eyes coordinates. Center LEDs around the lens are used to work with light pupil. The lighting current levels are adjustable.

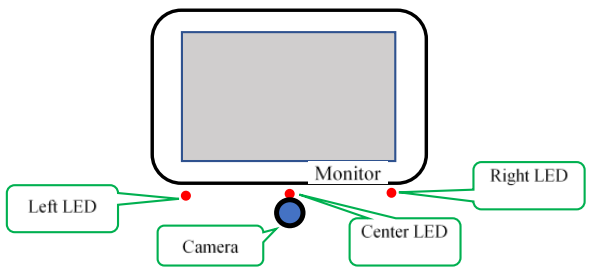


Fig. 3 Device layout diagram.

The gaze detection system used a fully programmable camera with USB 3.0 output and frame size up to 1440×1080 pixels. Most of the frame time on the

computer is used to take the image from the camera. There is no threading parallelization.

The software modules are written in C++, image processing was performed using the OpenCV library [12].

The determination of the pupil center was carried out in fragments of about 350×240 pixels, including the eye image (right or left by choice).

Since described image frame processing algorithms contain iterative procedures, the processing time depends on the scene in the frame. During the experiments, the procedure of calibration, calibration test and two seconds fix point hold was carried out. The sequence contains a sufficient variety of scenes. The real time frame processing is carried out to obtain the coordinates of the gaze fixation point and the frames recording at camera frame rate. Then, the recorded to a hard disk sequence may be processed from the disk at the fastest speed for a computer. By disabling the given algorithm, it is possible to estimate the average running time of the algorithm by the difference in processing time.

Frame file reading and entire image processing lasts about 8 ms on a 3.6 GHz processor, and the pupil center coordinates are obtained in an average of 1.2 ms. Depending on the image quality, the edge points outliers cutoff time by the RANSAC algorithm may be significantly increased in some frames, but the image arrays buffering evens out such deviations. Frame loss was also monitored. The system was tested at frequencies of 50 Hz and 100 Hz. At a frequency of 200 Hz, the entire frame time is occupied by the exchange with the camera and processing in real time is impossible. Executing the program in multiple threads allows you to bypass these limitations.

With a camera operating frequency 50 Hz, the transfer of the gaze fixation point from one monitor corner to another takes 2–3 frames. The eye is blurred and the frames have to be discarded. At a frequency 100 Hz, one image is blurred, and the pupil center position is determined on it, albeit with an error.

During the processing a real sequence, it is impossible to separate the algorithm operation influence error and fast eye movements. The system noise effect on the accuracy of the ellipse center coordinates determination was evaluated on a sequence formed from one real frame with different realizations of noise. The noise level, estimated from the difference between adjacent real frames, is 1.37 image sampling level. The ellipse center coordinates standard deviation Xe and Ye for 100 sequence frames at different noise levels is given in the Table 1.

Table 1 shows that stability is maintained up to high noise levels. When operating at a frequency 100 Hz, the noise level is slightly higher, because when the exposure time is decreased, the camera gain must be increased.

The system operation was tested on operators of different ages, different irises colors, and different pupil sizes both in laboratory and in the field.

Table 1 The noise value effect on the accuracy on the pupil center coordinates estimating.

Noise STD	Xe STD, pix.	Ye STD, pix.
1.0	0.06	0.06
2.0	0.09	0.07
3.0	0.14	0.13
4.0	0.37	0.24
8.0	0.34	0.29

4 Discussion

The well-known algorithm for pupil finding and determining its center coordinates Starburst [13] was developed for a head-mounted device. The MatLab version works well but slowly. There is approximately one second per frame of the camera image. A simplified version in C++ manages to process at 50 fps frame rate. Nevertheless, the pupil's border is very noisy because the radius derivative is evaluated in 4–6 pixels increments to highlight the level increment at low contrast.

Attempts to speed up the detection for the pupil center have been made several times. For example, in Ref. [14], the pupil contour is approximated by a sinusoid (SET method). The comparison of the accuracy of determining the pupil center by the Starburst and SET methods is carried out. However, approximation methods generally use iterative approximation and are slow. The algorithm was tested on small images containing the eye area that is typical for head-mounted devices.

The proposed algorithm selects a smoother border that is close to the real one. However, it uses the starting point after corneal reflection highlighting. StarBurst can find the border without specifying the starting point but only in images slightly larger than the eye size. You still need to find the eye area and select a fragment.

The proposed algorithm works on the both light and dark pupil. Many algorithms work with light pupil. We focused on dark pupil option. The hardware implementation is simpler, does not require a small diameter lens with central LEDs around it. Only two side LEDs are required to calculate the 3D eye position. There is also no need to synchronize the illuminators switching with camera frame changes.

5 Conclusion

The proposed algorithm for the determination of the pupil center coordinates provides stable results with a small scatter. The system was tested at frame rates of 50 and 100 Hz. The algorithm can be used at higher camera frequencies when using a camera with a higher channel bandwidth. Frames image processing in parallel with obtaining the next frame will also allow the pupil center coordinates assessing at higher frequencies.

It is also necessary to reduce computational resources requirement of the cornea reflection extraction and selection algorithm, which takes up most of the processing time.

As already mentioned, the main requirement is the IR illumination presence, which increases the contrast between the pupil and the iris. Hence the main limitation: the direct sunlight exposure lack. The use of the system is limited to rooms and moving objects with closed volumes.

A free head position reduces operator fatigue. In medical applications, it allows the study of patient behavior *in vivo*.

Disclosures

All authors declare that there is no conflict of interests in this paper.

Acknowledgements

The Ministry of Education and Science of Russia (Project 121022000116-0) financially supported this work.

The authors are grateful to the staff of the Branch of the Institute of Semiconductor Physics SB RAS 'DTIAM' for cooperation.

References

1. P. Biswas, J. DV, "Eye Gaze Controlled MFD for Military Aviation," In 23rd International Conference on Intelligent User Interfaces, 7–11 March 2018, Tokyo, Japan, 79–89 (2018).
2. J. P. Hansen, A. Alapetite, I. S. MacKenzie, and E. Møllenbach, "The use of gaze to control drones," Proceedings of the ACM Symposium on Eye Tracking Research and Applications, 27–34 (2014).
3. T. E. Petrova, E. I. Riekhakaynen, and V. S. Bratash, "An Eye-Tracking Study of Sketch Processing: Evidence From Russian," Frontiers in Psychology 11, 297 (2020).
4. E. A. Novikov, I. A. Vakoliuk, R. D. Akhapkin, I. A. Varchak, I. G. Shalanginova, D. A. Shvaiko, and E. A. Budenkova, "Automation method of computer oculoghaphy for research of the central nervous system based on passive video analysis," Machine Learning and Data Analysis 1(12), 1–12 (2015).
5. L. Cercenelli, E. Marcelli, "Eye Tracking in Ophthalmology: A Glimpse Towards Clinical Practice," EC Ophthalmology ECO 01, 16–18 (2017).
6. P. Chandon, J. W. Hutchinson, E. T. Bradlow, and S. H. Young, "Measuring the Value of Point-of-Purchase Marketing with Commercial Eye-Tracking Data," SSRN Electronic Journal (2007).
7. R. S. Hessels, C. Kemner, C. van den Boomen, and I. T. C. Hooge, "The area-of-interest problem in eyetracking research: A noise-robust solution for face and sparse stimuli," Behavior Research Methods 48, 1694–1712 (2016).
8. D. S. Raupov, O. O. Myakinin, I. A. Bratchenko, V. P. Zakharov, and A. G. Khramov, "Multimodal texture analysis of OCT images as a diagnostic application for skin tumors," Journal of Biomedical Photonics & Engineering 3(1), 010307 (2017).
9. M. A. Fischler, R. C. Bolles, "Random Sample Consensus: A Paradigm for Model Fitting with Applications to Image Analysis and Automated Cartography," Communications of the ACM 24(6), 381–395 (1981).
10. A. Fitzgibbon, M. Pilu, and R. B. Fisher, "Direct least square fitting of ellipses," IEEE Transactions on Pattern Analysis and Machine Intelligence 21(5), 476–480 (1999).
11. Satoshi Suzuki, K. Abe, "Topological structural analysis of digitized binary images by border following," Computer Vision, Graphics, and Image Processing 30(1), 32–46 (1985).
12. OpenCV (accessed 24 May 2021) [https://opencv.org/].
13. D. Li, D. J. Parkhurst, "Starburst: A robust algorithm for video-based," Elselvier Science (2005).
14. A.-H. Javadi, Z. Hakimi, M. Barati, V. Walsh, and L. Tcheang, "SET: a pupil detection method using sinusoidal approximation," Frontiers in Neuroengineering 8, 4 (2015).

Registration of Regeneration in Planarians from Photographic Images

Kharlampiy Tiras[1,2*], Leonid Mestetskiy[3,4], Svetlana Nefedova[1,2], and Nikita Lomov[4]

[1] Institute of Theoretical and Experimental Biophysics of the Russian Academy of Sciences, 3 Institutskaya str., Pushchino 142290, Moscow Obl., Russian Federation

[2] Pushchino State Institute of Natural Science, 3 Prospect Nauki, Pushchino 142290, Moscow Obl., Russian Federation

[3] Lomonosov Moscow State University, GSP-1, Leninskie Gory, Moscow 119991, Russian Federation

[4] Federal Research Centre "Computer Science and Control" of the Russian Academy of Sciences, 44 Vavilova str., block 4, Moscow 119333, Russian Federation

*** e-mail:** tiras1950@yandex.ru

Abstract. In this study, an approach to constructing a mathematical model for quantifying the dynamics of regeneration of planarian flatworms in biological experiments is considered, based on an analysis of a series of digital microscopic images. A method is proposed to describe the body shape of a planarian using a continuous morphological model, based on the concept of a medial representation of the worm's silhouette. The silhouette in this case is a polygon approximating the contours of the planarian's body. The medial representation of the figure includes a medial axis and a radial function that describes the width of the figure relative to the medial axis. We propose a set of morphological criteria for assessing the dynamics of regeneration based on a continuous morphological model and present the results of computational experiments. © 2021 Journal of Biomedical Photonics & Engineering.

Keywords: planarians; digital morphometry; medial representation; image skeleton.

Paper #3430 received 25 May 2021; revised manuscript received 6 Sep 2021; accepted for publication 6 Sep 2021; published online 30 Sep 2021. doi: 10.18287/JBPE21.07.030303.

1 Introduction

The progress of modern biology is determined by the development of digital technologies for the creation and analysis of lifetime images of biological objects. A new science of digital biology is being formed as a synthesis of biology and mathematics, which reflects the process of transition of the description of biological objects "from a verbal one to a digital one". The results obtained in this new biological science can be verified by comparing the data generated by different software products, implementing mathematical models, hypotheses, methods and algorithms, on the same group of images.

An example of such a process is the development of a complex of methods for the dynamic morphometry of regeneration in planarian flatworms. Their flat body structure and ability of smooth ciliary movement allow researchers to obtain accurate lifetime images of the planarians that can be analysed by applying various criteria [1–2]. Lifetime photo capture of the regeneration process allows its registration in the same group of animals, which minimises the number of animals required in each experiment and increases the quality of the experiments themselves.

To minimise labour costs and human influence on the outcome, the tools for calculating the required criteria automatically are being developed [3–4]. The latter of these methods are based on the analysis of the planarian shape from images using continuous morphological models [5–6].

Planarians have a unique ability to regenerate: they are able to regrow any lost part of their body in a very short time. After removal of the head end of the body including the nerve ganglion, the regeneration process takes from 5 to 25 days. The special significance of this biological model of regeneration lies in the possibility of extrapolating the processes of cell proliferation and differentiation, and the processes of growth and morphogenesis, at the level of the whole organism [1]. This opens up prospects for the control of cellular processes at the macro level, which makes it possible to

obtain a complete quantitative description of the regeneration process *in situ*.

Owing to their ability to regenerate quickly, planarians are often used as a model test object. However, progress in this area has been limited by the laboriousness of the procedure for creating equivalent experimental groups. Therefore, the creation of a system for the automated determination of the dimensional characteristics of planarians is very urgent.

2 Materials and methods

2.1 Biological model

This study was carried out on planarians of the asexual race *Girardia tigrina*, of which a population has been established since 1970 at the Institute of Biophysics of the USSR Academy of Sciences, and the Institute of Cell Biophysics and the Institute of Theoretical and Experimental Biophysics of the Russian Academy of Sciences at the Pushchino Scientific Centre. The classic format of an experiment on planarian regeneration consists of cutting off the head end of the worm (in the region of the auricles). This operation was carried out with the aid of a Zeiss Stemi 2000 binocular microscope equipped with an AxioCam MRc video camera (1.2 MP) in non-sterile conditions. The process of restoration of the planarian body was observed by the method of lifetime digital morphometry [1–2].

The effect of the biologically active peptide CLV3 (amino acid composition: RTVPSGPDPLHH), a plant growth stimulator isolated from the roots of *Arabidopsis thaliana*, in solutions at concentrations of 10^{-9} M and 10^{-12} M, was studied [7].

Regenerating planarians moving randomly in the aquatic environment were photographed daily using a digital microscope. The body shape of a planarian is well described by a two-dimensional image in a photograph; therefore, a morphological approach to assessing the rate of regeneration based on an analysis of the size and shape of the worm's body is very effective.

After the transection, within 72 h the regrowth of a new head part of the body (regeneration blastema) becomes visible, which is not covered with pigment cells in the first 3–4 days after surgery (Fig. 1). This makes it possible to use the photocontrast between old (pigmented) and new (optically transparent) body parts of the planarian regenerant to determine the regrowth boundary during the interactive process of analysing the planarian image.

In order to measure and analyse the rate of the planarian recovery process, it is necessary to obtain a quantitative criterion that makes it possible to assess how much the parameters of experimental animals have changed over certain time intervals. Previously, the use of software products made it possible to accurately estimate the total size of the growing part of the planarian body and calculate the regeneration criterion as the ratio of the area of the blastema to the total area of the planarian body [1–2]. However, the problem of determining the shape parameters of the growing part of the body during regeneration remained unresolved. This indicator of shape change – that is, morphogenesis – is necessary to describe the growth and morphogenesis processes during regeneration completely. Solving this problem has been complicated by a number of objective factors [2, 5].

The quantitative registration of changes in the body shape of a planarian is complex for the following reasons:

- the body shape differs quite widely in individual worms, and therefore, the process of morphogenesis also has individual characteristics;
- when cutting a worm, it is not possible to ensure absolutely the same position of the cut in different individuals, which also adds individual characteristics to the regeneration process; and
- in the course of regeneration, the overall size of each worm decreases because the restoration of its body occurs through internal transformation of tissue rather than from external nutrition.

Large groups of worms are used in experiments to obtain representative estimates of the dynamics of planarian regeneration. Thus, the task is to assess the dynamics of shape change for a group of 20–30 individuals within 10–25 days, based on observing the regeneration process by registering images in the field of view of the microscope. For the prompt processing of the corresponding array of photographs and calculation of the blastema area, it is necessary to automate this process.

2.2 Method for assessing the morphogenesis of planarian regeneration

In this work, we propose an approach to assessing the dynamics of planarian regeneration, based on the analysis of the shape of flatworms from a sequence of photographs [2, 6, 7]. Within the framework of this

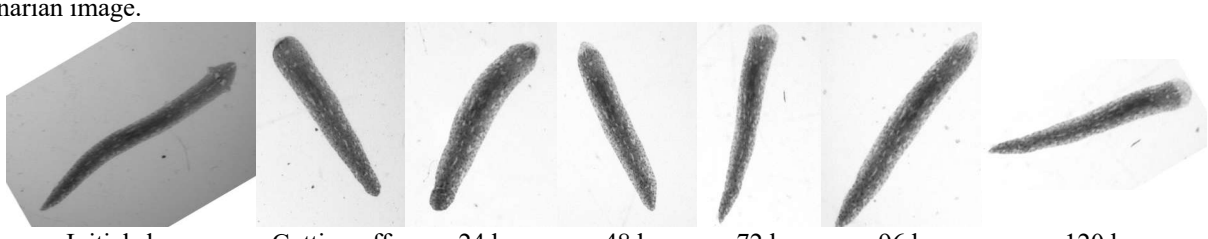
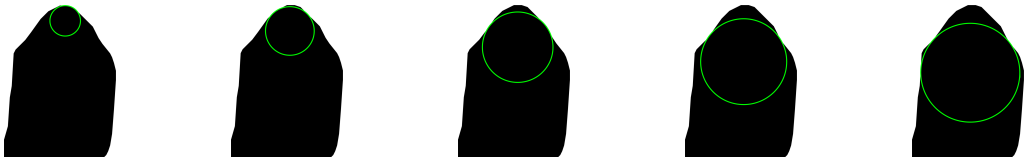


Fig. 1 Intact and regenerating planarians Girardia tigrina at different times after surgery.



24 h 48 h 72 h 120 h 144 h

Fig. 2 Dynamics of regrowth of the anterior end of the regenerative blastema with time elapsed since the head was severed. The size of the images in pixels is specified.



r = 8 px 13 px 18 px 22 px 26 px

Fig. 3 Inscription of circles touching with the border of the body into the blastema.

approach, we developed a criterion for quantifying the rate of change in the shape of planarians, as well as a numerical method for calculating this estimate, based on a sequence of images for the group of planarians we used in our experiment.

The initial data constituted photographic images of planarians, taken daily within 1–2 weeks after the planarians' heads were severed. Because it was impossible to fix the position of the planarians' bodies, the animals were presented in the photographs in arbitrarily bent positions.

The method we proposed was to construct a so-called morphological model of the planarian body based on the medial representation of its shape as a figure with a skeleton and radial function [8–9]. A skeleton is a set of medial axes in a figure, consisting of centres of all the circles inscribed in the figure. The radial function is defined at each point of the skeleton and is equal to the radius of the inscribed circle centred on that point.

The morphological model was designed to quantify the rate of regeneration. In the course of regeneration, the "regrowth of the head" of the planarian takes place. In particular, this process is expressed in a change in the shape of the head end of the worm. Fig. 2 shows how the shape of the head end changes. It is clearly seen that, over time, the change in shape is expressed in the elongation of the head, the formation of a pointed apex – apex of the blastema – as a result of which the head becomes more and more triangular. The morphological model was designed to assess the geometric characteristics of the planarian's body: the elongation of the head end and the "triangularity" of the head.

To register the degree of regeneration as a quantitative indicator, we needed to establish geometric criteria that would take into account the degree of sharpening, or increase in acuteness, of the angle of the blastema apex. This quantitative indicator had to be sensitive to the change in the angle during the regrowth of the worm's head.

3 Morphological model and criteria

3.1 Morphological model of planarian shape

The idea of constructing a morphological model is shown in Fig. 3. Circles with two or more points of contact with the boundary of the planarian's silhouette are inscribed in the contour of the worm's silhouette, and the points of contact lie within the area of the worm's head.

The inscribed circles can be of different sizes, determined by the radius r. In accordance with these dimensions, the circles are located at different depths relative to the apex of the blastema – the end point of the head. We used two functions as an indicator of head elongation: the area of the apex of the blastema $S(r)$ and the length of the apex of the blastema $L(r)$. The meaning of these values is illustrated in Fig. 4.

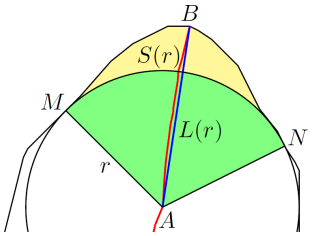
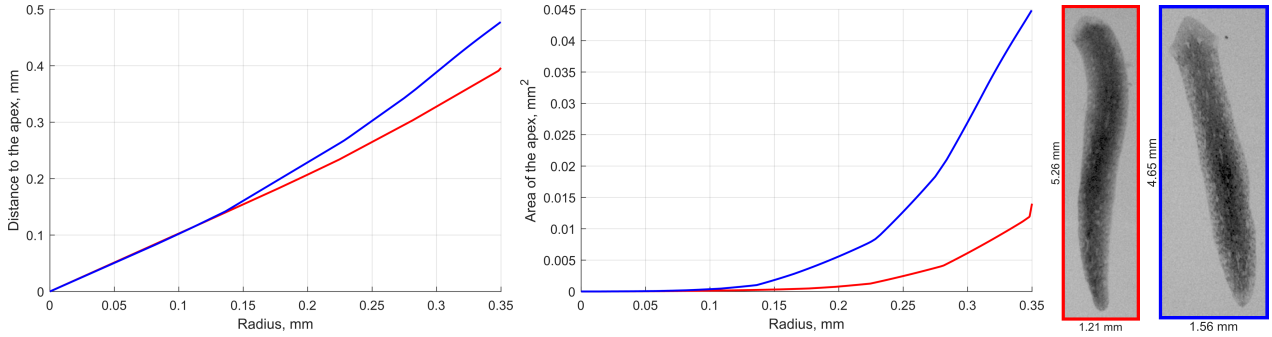


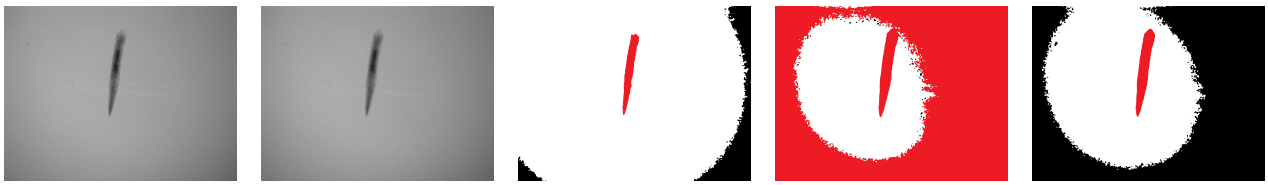
Fig. 4 Scheme of the morphological model.

To determine the value of the function describing the area of the blastema apex at point A, we calculated the tangency points of the circle centred on A inscribed in the boundary polygon. In Fig. 4, these are points M and N. Using points A, M and N, as well as the vertex of the blastema B and the vertices of the boundary polygon, we calculated the area of the polygon $AMBN$, and that of the



(a) (b) (c) (d)

Fig. 5 Dynamics of the length and area functions of the blastema apex $L(r)$ (a) and $S(r)$ (b) respectively and the source images (c, d). The colour of the image frames corresponds to the colour of the chart lines.



(a) (b) (c) (d) (e)

Fig. 6 General sequence of operations for constructing a morphological model of the length and area of the blastema apex. See the list above for a description of each stage.

circular sector AMN, shown in the Fig. 4 in green. The area of the apex of the blastema $S(r)$, shown in yellow in the Fig. 4, is equal to the difference between these two areas. The length of the apex of the blastema $L(r)$ is equal to the distance between points A and B and is shown in blue. The main axis (locus of the inscribed circles' centres) is shown in red.

The functions of the length and area of the blastema apex $L(r)$ and $S(r)$ are monotonic; examples of their plots are shown in Fig. 5. Here, the functions are constructed for two images of planarians. The image in the red frame was taken on the second day of regeneration, and the image in the blue frame was taken on the ninth day. The left diagram shows the plots of the blastema apex length, and the right diagram shows the area of the blastema apex. It can be seen clearly from the diagrams that the blue curves describing the later stage of regeneration dominate the red curves belonging to the earlier stage. This is quite consistent with our visual observation of the blastema apex's elongation and the resulting increase in its length and area.

The general sequence of how we segmented (selected) each planarian image – i.e., built a binary silhouette of the planarian – is as follows and is shown in Fig. 6:

a) obtaining a grayscale image containing the individual planarian;

b) smoothing this image with a Gaussian filter with standard deviation $\sigma = 3$;

c) applying threshold binarization to the image so that 10% of the pixels turn black and determining the base of the connected component of the planarian – the maximum connected component that does not touch the frame boundaries (red area);

d) determining the limit value of the threshold t_{max} by increasing the threshold for binarization until the connected component of the planarian touches the frame borders; and

e) applying binarization to the image with a threshold of $t_{max} - 4$ and selecting of a connected component containing the base.

The general sequence of how we built the morphological model of a planarian is as follows and shown in Fig. 7:

a) approximating the binary silhouette of the planarian (Fig. 7a) by a polygon (Fig. 7b);

b) building the skeleton and radial function of the polygon (Fig. 7c);

c) pruning the skeleton – i.e., cutting off insignificant branches – according to the algorithms from Ref. [8] with maximal possible deviation of 20 pixels from the original silhouette (red line in Fig. 7d);

d) searching for potential apexes of the blastema – i.e., constructing the rays tangent to the end vertices of the pruned skeleton (dashed lines in Fig. 7d) and determining contour points with the most distant projections on these rays (blue points);

e) completing the pruned skeleton to the main axis of the planarian by paths to the potential apexes in the non-pruned skeleton and determining the path lying in the head by the greater average radius $\frac{\int r(l)dl}{\int dl}$ (Fig. 7e); and

f) determining the reference circle by moving along the pruned skeleton from the terminal vertex in the head (where its radial function is r_{cut}) to a distance of $0.2 * r_{cut}$.

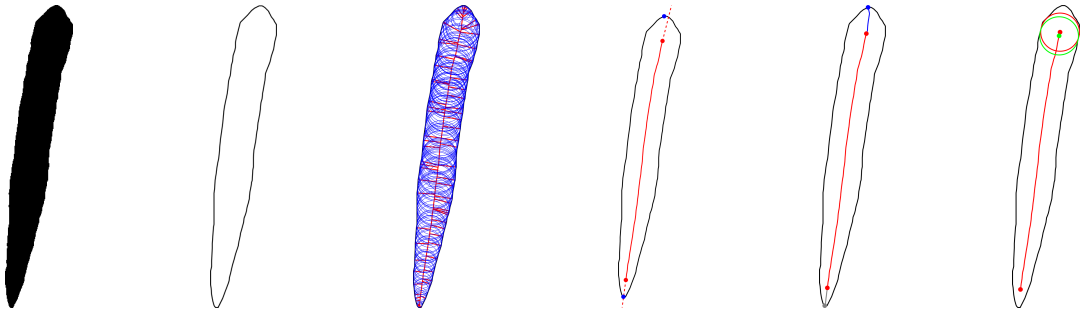


Fig. 7 General sequence of operations for constructing a morphological model of the length and area of the blastema apex. See the list above for a description of each stage.

The length and area functions of the blastema apex $L(r)$ and $S(r)$ were calculated using a continuous morphological model. Further, these functions were normalized by taking into account the radius of the reference circle $\bar{r}$: $\tilde{L}(\rho) = \frac{L(\rho\bar{r})}{\bar{r}}$, $\tilde{S}(\rho) = \frac{S(\rho\bar{r})}{\bar{r}^2}$. Note that after normalization, the arguments and the values of these functions become dimensionless quantities (arbitrary units). The constructed morphological model was further used to determine the first point with the given radius on the main axis, following from the apex. Since each edge of the skeleton consists of points equidistant from two sites (edges or concave vertices) of the boundary, this model allowed us to directly find tangency points M and N, as shown in Fig. 4, and to estimate the length and area of the blastema apex from the change in the radial function along the axis. The procedures described above were implemented in C++, MATLAB was used to analyse the results.

3.2 Morphological evaluation of a group of planarians

The functions $L(r)$ and $S(r)$ were calculated sequentially at discrete points of the axis, selected with a certain step. Thus, the functions of the length and area of the blastema apex were calculated for each planarian from the group. Group functions could be obtained as averages over a group of m planarians:

$$\hat{L}(\rho) = \frac{\sum_1^m \tilde{L}_i(\rho)}{m};$$
$$\hat{S}(\rho) = \frac{\sum_1^m \tilde{S}_i(\rho)}{m}, \quad (1)$$

where $\tilde{L}_i(\rho)$ and $\tilde{S}_i(\rho)$, $i = 1, \ldots, m$ are the normalized length and area of the blastema apex of the i-th planarian from the group. Planarians were photographed in the resolution of 97 pixels per mm (2413 ppi), the sizes of individuals varied in the range of 2 to 6.7 mm (length) and in the range of 0.9 to 3.6 mm^2 (area). The diagram in Fig. 8 illustrates some of the experimental results.

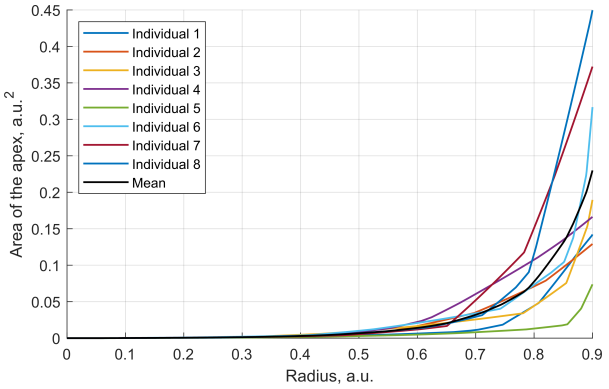
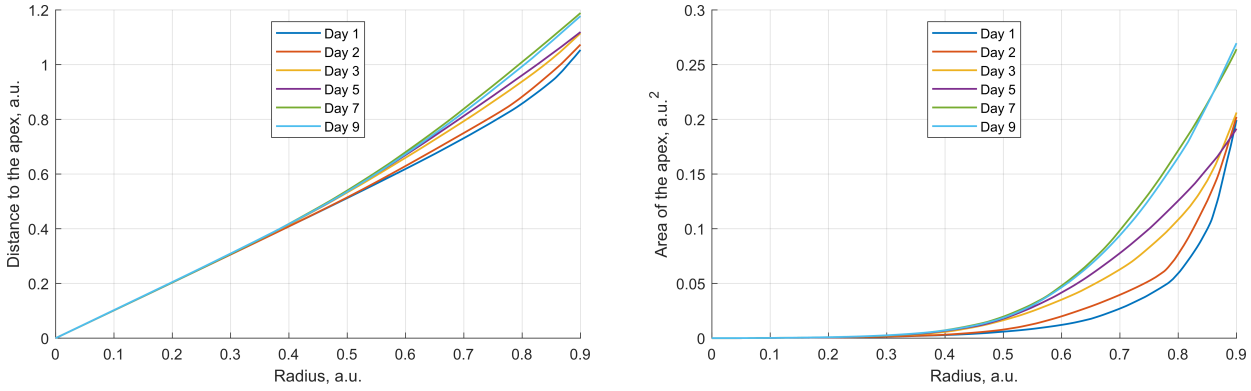


Fig. 8 Diagram showing the dependence of the area of the blastema apex on the radius of the inscribed circle r, for different individuals from the same group.

As can be seen from the diagram, these curves for individual planarians vary significantly. However, the average curves calculated from them, which characterize a group of planarians, made it possible to assess the main quantitative regularities of the regeneration process. This can be seen in the two diagrams in Fig. 9, which show integral curves for the same group of 20 planarians, plotted from images in the first 9 days after regeneration. The curves show the growth of the planarians' heads and provide quantitative estimates of this growth.

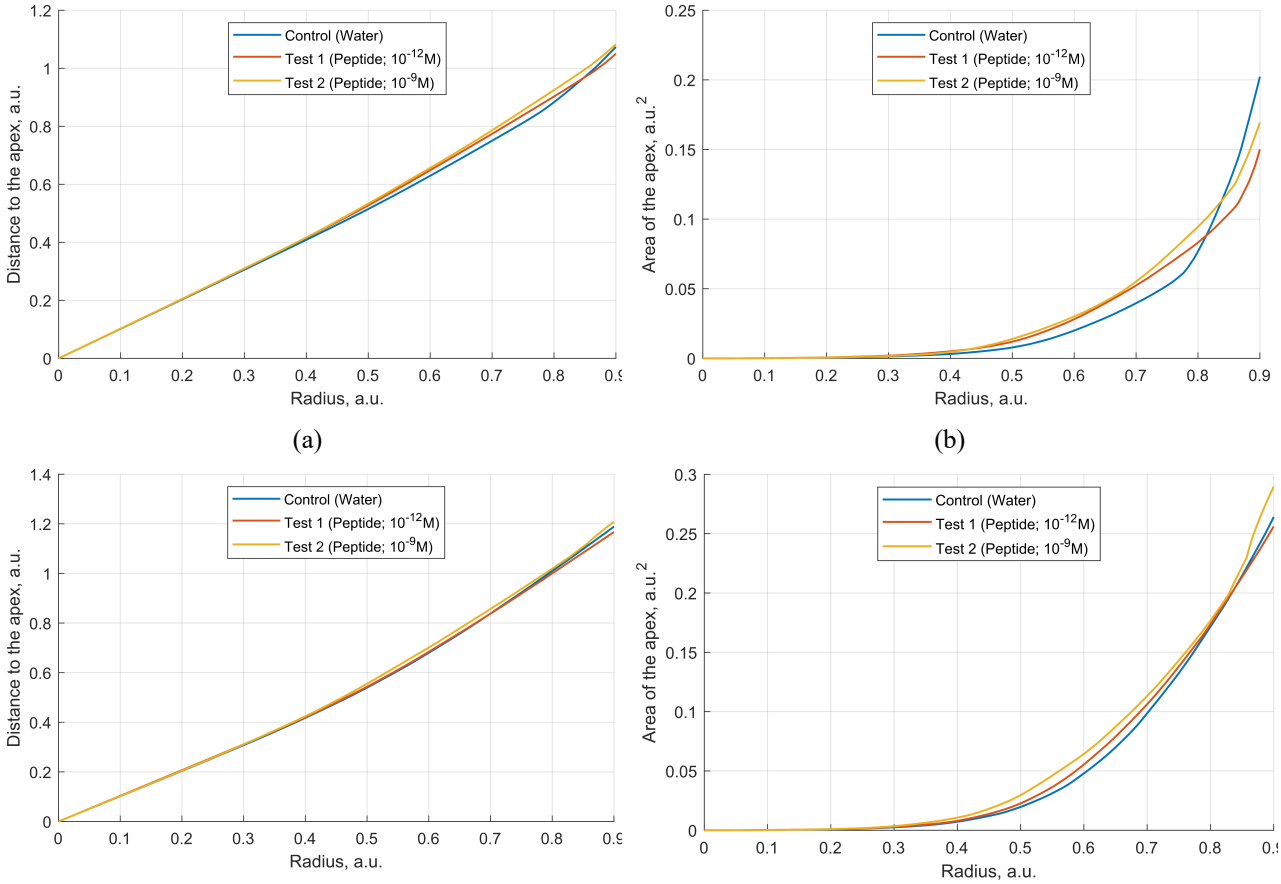
In Fig. 10, the diagrams show the results of our experiments to assess the rate of regeneration of planarians placed in various media. Groups of 20 planarians each were studied in pure water (control group) and in plant growth stimulant pCLV3 peptide solutions at concentrations of 10^{-9} M and 10^{-12} M (test groups). All graphs are based on images taken on the third day of the regeneration process. These diagrams confirm that it is fundamentally possible to assess the dynamics of planarian morphogenesis, which are dependent on various external physical and chemical factors. Our approach makes it possible to obtain reliable quantitative estimates of this dependence.

The graphs are consistent with the hypothesis that the plant growth stimulant pCLV3 peptide also stimulates the regeneration of lost tissue in planarians [10].



(a) (b)

Fig. 9 Integral curves of the length (a) and area (b) of the blastema apex for the same control (without peptide) group of 20 planarians, plotted from images in the first 9 days of regeneration.



(a) (b)

(c) (d)

Fig. 10 Integral curves of the length (a, c) and the area (b, d) of the blastema apex for the control group and two experimental groups of 20 planarians each, plotted from images on the 2nd (a, b) and 5th (c, d) days of regeneration.

4 Conclusion

The results of this study demonstrated that it is fundamentally possible to quantify the rate of regeneration in flatworms from a series of images. The method we developed for obtaining such estimates is based on the morphological analysis of images: segmentation of the body of a planarian, approximation of the silhouette by a polygon with the highest possible accuracy for a digital image, obtaining a medial representation of the silhouette and calculating curves based on it, and showing the dynamics of changes in the worms' body shapes for different periods of time elapsed since the beginning of the regeneration process. The quantitative estimates we obtained allowed a clear and meaningful interpretation, which in turn made it possible to assess their reliability. The method we proposed was

based on the construction of a continuous morphological model, which made it possible to ensure high computational efficiency of this solution and convenient, meaningful visualisation. The approach described here is being implemented by means of corresponding software and has found application in practical research. Further development of non-contact, non-invasive approaches to assessing the processes of morphogenesis of planarians can be possible using such optical methods as hyperspectral technique [11] and Raman spectroscopy [12], which are now widely used to analyse the state of biological tissues.

Disclosures

All authors declare that there is no conflict of interests in this paper.

Acknowledgements

This work was funded by Russian Foundation of Basic Research Grant No. 20-01-00664.

References

1. K. P. Tiras, V. I. Khachko, "Criteria and stages of regeneration in planarians," Ontogenez 21(6), 620–624 (1990) [in Russian].
2. K. P. Tiras, O. N. Petrova, S. N. Myakisheva, A. A. Deyev, and K. B. Aslanidi, "Minimizing of morphometric errors in planarian regeneration," Fundamental Research 2(7), 1412–1416 (2015) [in Russian].
3. S. Flygare, M. Campbell, R. M. Ross, B. Moore, and M. Yandell, "ImagePlane: an automated image analysis pipeline for high-throughput screens using the planarian Schmidtea mediterranea," Journal of Computational Biology 20(8), 583–592 (2013).
4. N. Macleod, "On the Use of Machine Learning in Morphometric Analysis," Biological Shape Analysis: Proceedings of the 4th International Symposium, World Scientific Publishing, 134–171 (2017).
5. L. M. Mestetskiy, K. P. Tiras, "Morphological assessment of the dynamics of regeneration of planarians from photographic images," Mathematical Methods for Pattern Recognition 18(1), 120–121 (2017) [in Russian].
6. K. P. Tiras, L. M. Mestetskiy, "Normalization of planarian images by the fat curve method in biological research," in 17th International Conference on Mathematical Methods for Pattern Recognition, Svetlogorsk, 19–25 September 2015, 182–183 (2015) [in Russian].
7. K. Tiras, U. Vorobeva, K. Novikov, V. Voeikov, V. Emelyanenko, G. Davidova, and A. Skripnikov, "Peptide regulation of plant and animal morphogenesis: general mechanisms and specificity of action," IOP Conference Series: Materials Science and Engineering 487, 012020 (2019).
8. L. M. Mestetskiy, Continuous morphology of binary images: figures, skeletons, circulars, Moscow, Fizmatlit (2009) [in Russian]. ISBN: 978-5-9221-1050-1.
9. R. Gonzalez, R. Woods, Digital Image Processing, 4th ed., Pearson, India (2018).
10. X. Wang, M. G. Mitchum, B. Gao, C. Li, H. Diab, T. J. Baum, R. S. Hussey, and E. L. Davis, "A parasitism gene from a plant-parasitic nematode with function similar to CLAVATA3/ESR (CLE) of Arabidopsis thaliana," Molecular Plant Pathology 6(2), 187–191 (2005).
11. V. P. Sherendak, I. A. Bratchenko, O. O. Myakinin, P. N. Volkhin, Y. A. Khristoforova, A. A. Moryatov, A. S. Machikhin, V. E. Pozhar, S. G. Kozlov, and V. P. Zakharov, "Hyperspectral in vivo analysis of normal skin chromophores and visualization of oncological pathologies," Computer Optics 43(4), 661–670 (2019).
12. L. Bratchenko, I. Bratchenko, Y. Khristoforova, D. Artemyev, Y. Konovalova, P. Lebedev, and V. Zakharov, "Raman spectroscopy of human skin for kidney failure detection," Journal of Biophotonics 14(6), e202000360 (2020).

Numerical Modeling of Radiation Focusing by Dielectric Microcylinders with Several Layers

Alexandra A. Savelyeva[1,2*] and Elena S. Kozlova[1,2]

[1] IPSIRAS – branch of the FSRC "Crystallography and Photonics" RAS, 151 Molodogvardejskaya str., Samara 443001, Russia

[2] Samara National Research University, 34A Moskovskoe Shosse, Samara 443086, Russia

*** e-mail:** lexis2450@gmail.com

Abstract. In this paper, the light focusing by dielectric microcylinders with several layers was numerically studied by using the finite element method implemented in COMSOL Multiphysics. Different materials for the top layer were proposed during the research (refractive indices are 1.59, 1.8, 1.9) while the core was proposed from fused silica glass (refractive index is 1.45). It was shown that the dielectric shell allows to increases the maximum intensity of the formed photonic nanojet. Choosing the design of a two-layered microcylinder it is possible to form a compact focal spot (TE-polarization) or increase the length of the produced photonic nanojet. Obtained results were verified by another software package FullWAVE which implements a finite difference time domain method. The simulation results are in good agreement. © 2021 Journal of Biomedical Photonics & Engineering.

Keywords: two-layered dielectric microcylinder; photonic nanojet; sharp focusing; FDTD-method; FEM-method.

Paper #3434 received 25 May 2021; revised manuscript received 21 Sep 2021; accepted for publication 22 Sep 2021; published online 30 Sep 2021. doi: 10.18287/JBPE21.07.030304.

1 Introduction

Compression of light into a narrow beam is one of the priority tasks in nanophotonics [1–3]. Ultra-narrow light spots or nanojets are widely used in modern optical instrumentation. The problems of nanojets formation and optimization of their parameters are being actively studied by the world scientific community due to their importance in different areas [3–5] and mostly in biomedicine [6–8]. They are used for micromanipulation [9, 10], optical tweezers [11–13], for fluorescence enhancement in Raman spectroscopy [14], in histological studies [15], *in vivo* application [16].

A nanojet is an ultra-narrow light spot spreading over several wavelengths [17–20]. The main parameters which are primarily of interest to researchers are the maximum intensity, the distance from the optical element to the peak of the intensity, the full width (FWHM) and depth (DOF) at half maximum of intensity. In their research, scientists try to optimize the nanojet in such a way as to obtain the most compact light spot with maximum intensity in focus and maximum length. There are many articles on the generation and optimization of nanojets using different optical elements [17–26]. In study [18] authors report about narrow photonic nanojet which is formed by an engineered two-layer microcylinder of high refractive-index materials. Finite element analysis showed that under 632.8 nm illumination, the full width at half maximum of the beam waist can reach 87 nm. In Ref. [21], using numerical simulations it was shown that when focusing light with a wavelength of $\lambda = 550$ nm by a micro-flat-ended cylinder with a refractive index $n = 4$, the full width at half maximum can reach 70 nm. Using the COMSOL Multiphysics software package it was shown in Ref. [23], that a triangular prism made of quartz glass and illuminated by laser light with wavelength of 4 μm forms a focal spot the maximum intensity of which exceeds the intensity of the incident radiation for 5 times. The FWHM of obtained nanojet was 0.38λ. In Ref. [26], for the first time, authors numerically demonstrate that the size of the nanojet formed in the localized region of the dielectric mesoscale sphere can be significantly reduced by introducing a nanohole at its shadow surface.

The improvements are often made to the design of the focusing optical element for optimization of the nanojet parameters. For example, metal cores [27, 28] and shells [29, 30], multilayer dielectric structures [31, 32] can be used. Two types of spheres: an ordinary dielectric

sphere and a sphere with a metal core are considered in Ref. [27]. The best result in light focusing was achieved using a two-layered sphere. In Ref. [28], the authors proposed a method for light focusing by multilayer cylinders with metal shells made of gold, silver, and copper. It is shown that metal coatings affect the location of the nanojet. For a microcylinder made of gold and silver, a focal spot with FWHM = 293 nm was obtained. In Ref. [30], we proposed an unusual design of a polyester cylinder with silver film and a gap on the shadow side. A series of numerical simulations were carried out in which the hole diameter was varied. It was shown that a microcylinder with a radius of 2.1749λ and with a silver film of 90 nm and a hole of 100 nm formed a light field with a maximum intensity of 10.61 a.u. which is 1.4 times higher than the intensity of light field formed by the ordinary polyester cylinder. In Ref. [31] the authors consider five-layer cylinders as a focusing elements. The selection of radius and refractive indices was carried out using a genetic algorithm. The research showed that the parameters of the generated nanojets can be controlled by changing the focusing elements design. For example, a five-layer microcylinder designed in this study managed to generate an ultra-long nanojet with length of 107.5λ (λ = 632.8 nm).

In this paper, we investigate the focusing process of TE- and TM-polarized electromagnetic light with a wavelength λ = 633 nm by two-layered circular dielectric microcylinders. In the first part of the study, the influence of dielectric shell on photonic nanojet formation by using numerical experiments in COMSOL Multiphysics 5.1 which implements the finite element method (FEM) was evaluated. The two-layered structure of microcylinders is optimized. In the second part, the obtained results were verified by another software package FullWAVE 2020.03 which implements the finite difference time domain method (FDTD method). It showed good agreement with COMSOL Multiphysics.

2 Materials and methods

In our research, we discuss the process of linearly polarized laser light focusing by two-layered dielectric microcylinders. The wavelength λ was chosen equal to 633 nm. The total cylinder diameter is fixed at 2 μm, and the core diameter (D_{core}) is varied from 1.2 μm to 1.9 μm. The refractive index of the cylinder core is n_1, and the refractive index of the cladding is n_2. The numerical simulation scheme is shown in Figure 1, where D_{core} is the core diameter and D_{sh} is the shell diameter of cylinder.

This paper demonstrates the results of the numerical simulations obtained using the software package COMSOL Multiphysics which implements FEM [33, 34] for solving next wave equation:

$$\nabla \times \mu_r^{-1}(\nabla \times \boldsymbol{E}) - k_0^2\left(\epsilon_r - \frac{j\sigma}{\omega\epsilon_0}\right)\boldsymbol{E} = 0, \qquad (1)$$

where μ_r is the relative permeability, $\boldsymbol{E}$ is the vector of electric field intensity, k_0 is the free-space wavenumber, ε_r is the relative permittivity, j is the imaginary unit, σ the electrical conductivity, ω is the angular frequency of incident light, ε_0 is the permittivity of vacuum. This method is widely used in various studies of light focusing [35–37].

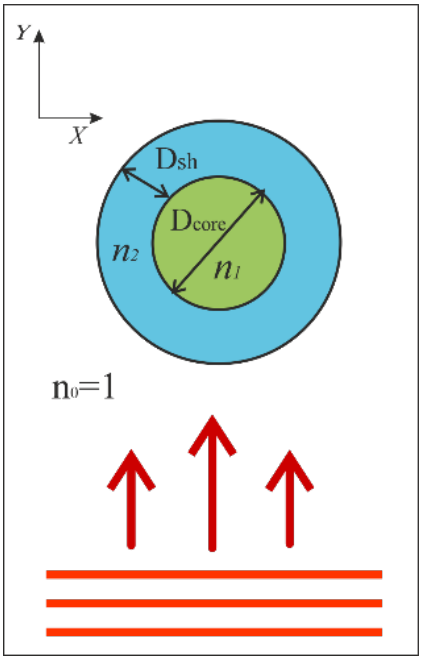


Fig.1 - Scheme of numerical simulation.

A triangular mesh with the following parameters were used in modeling: a step of λ/60 for areas where the refractive index changes and λ/40 for regions with constant refractive index. These steps provide numerical convergence (standard deviation is 0.001%).

After the main simulation results were obtained by using the COMSOL Multiphysics, a series of additional simulations was made for the cylinders with the best designs. For additional simulations FDTD-method implemented in the FullWAVE software package from RSoft Design Group was applied. This algorithm used the Maxwell's system of equations [38]:

$$\begin{cases} \frac{\partial \boldsymbol{D}}{\partial t} = rot\boldsymbol{H}; \\ -\frac{\partial \boldsymbol{B}}{\partial t} = rot\boldsymbol{E}, \end{cases} \qquad (2)$$

where $\boldsymbol{H}$ is vector of the magnetic field, $\boldsymbol{D}$ and $\boldsymbol{B}$ are vectors of the electric and magnetic induction.

FDTD method was firstly proposed by Kane S. Yee in Ref. [39]. Currently, this method is widely used by scientists in various studies, for example in Refs. [40 – 44].

The following parameters of a rectangular grid in space were used here: a 20 nm step along transverse and longitudinal coordinates. The temporal step $c\Delta t$ was chosen equal to 10 nm according to Courant condition. These steps ensure the convergence of the numerical method (the standard deviation is 0.001%). While analyzing simulation results the averaging of the intensity distribution for 10 periods was made.

3 Results and Discussion

3.1 Numerical simulation using FEM-method

In this section, the main study obtained by using numerical simulations in the software package COMSOL Multiphysics is presented. Firstly, TE-polarization is investigated. We considered microcylinders with core made of fused silica glass ($n_1 = 1.45$ [45]) and shell made of SiN ($n_2 = 1.9$ [46]). During the simulation results analysis, we evaluate the following parameters of the nanojet: the maximum intensity I_{max}, the focal length F, FWHM, and DOF, which are presented in Table 1.

It can be seen from Table 1 that the best design of a two-layered cylinder is the case when $D_{core} = 1.7$ μm. The results for this microclinder are marked as bold. Despite the fact that the maximum intensity of the nanojet is observed for a simple dielectric cylinder with a refractive index of $n_1 = 1.45$, a two-layer cylinder makes it possible to increase DOF by about 2 times. This fact can simplify the use of such nanojets in applications.

Table 1 Parameters of the focal spot formed by the two-layered microcylinders with $n_1 = 1.45$ and $n_2 = 1.9$.

D_{core}, μm	I_{max}, a.u.	DOF, λ	FWHM, λ	F, μm
2.0	7.97	0.78	0.37	0.02
1.9	5.10	0.91	0.43	0.13
1.8	3.44	1.32	0.54	0.21
1.7	4.81	1.66	0.47	0.07
1.6	**5.13**	**1.79**	**0.49**	**0.25**
1.5	2.87	2.35	0.59	0.62
1.4	2.51	2.05	0.67	0.52
1.3	2.83	2.23	0.77	0.60
1.2	2.51	2.05	0.67	0.82

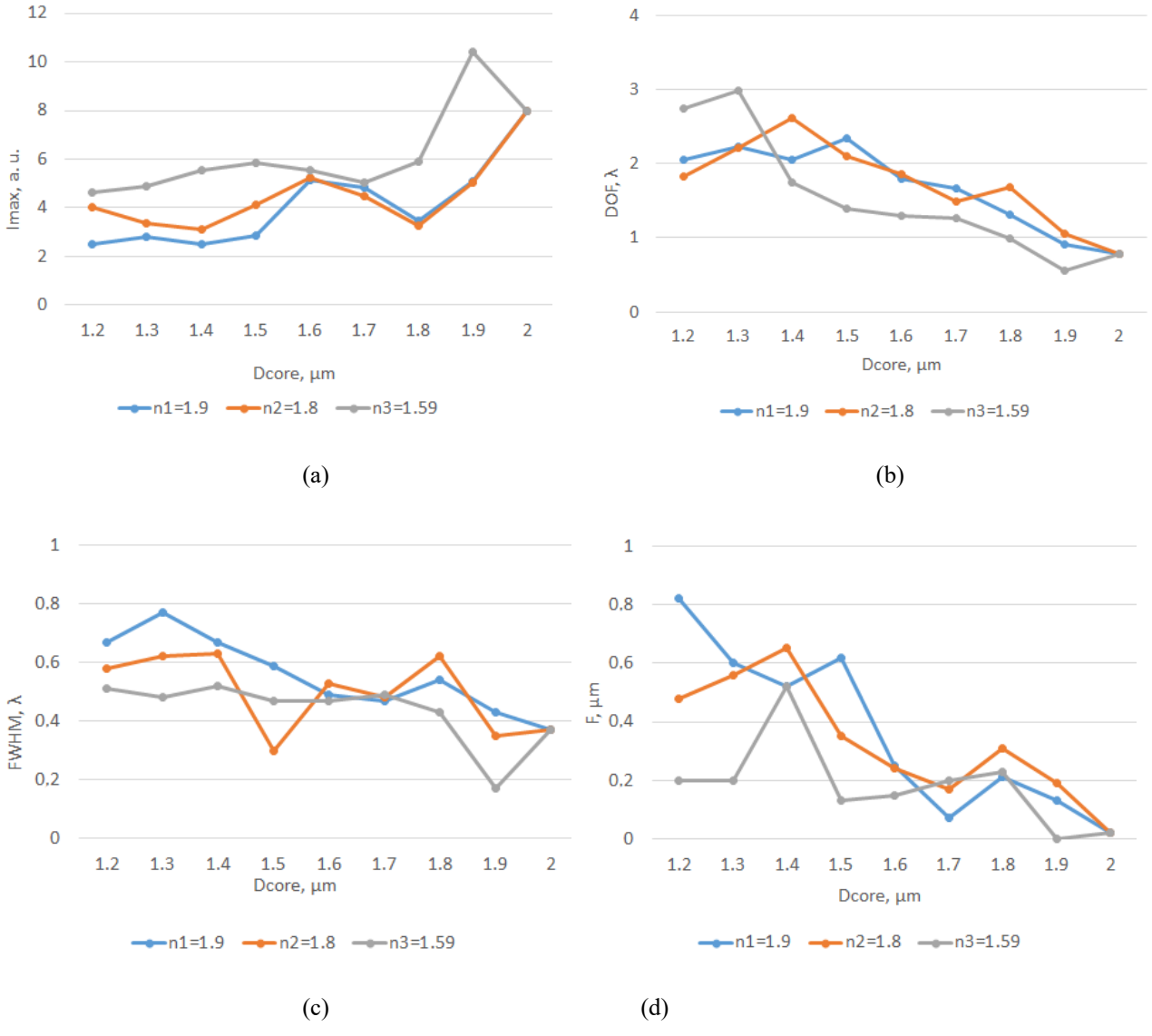


Fig. 2 Dependence of the I_{max} (a), DOF (b), FWHM (c), F (d) on the core diameter for TE-wave.

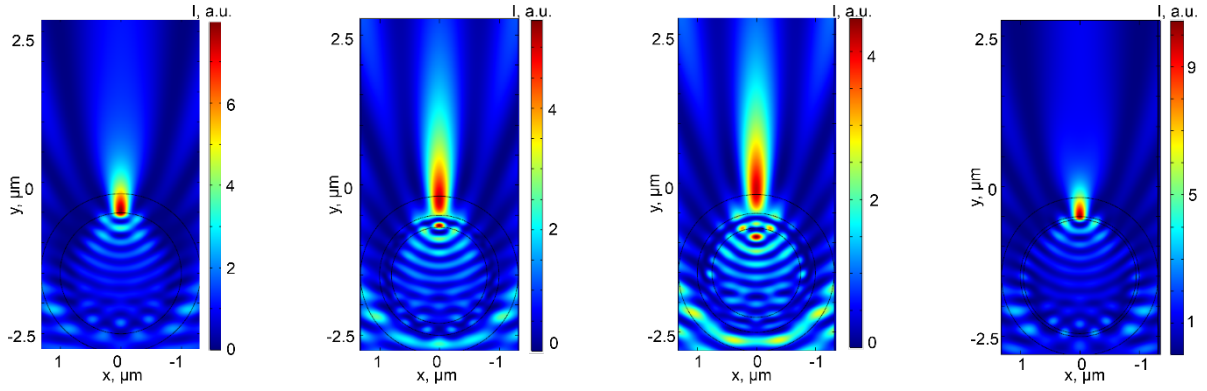


Fig. 3 The intensity distribution for ordinary microcylinder (a) and intensity distribution for two-layered microcylinders with n_2 =1.9 and D_{core} = 1.6 (b); n_2 =1.8 and D_{core} = 1.5 (c); n_2 =1.59 and D_{core} = 1.9 (d) illuminated by TE-wave.

Next, we propose the shell from titanium oxide-organic polymer (n_2 = 1.8 [47]). The obtained results are presented in Table 2.

Table 2 Parameters of the focal spot formed by the two-layered microcylinders with n_1 = 1.45 and n_2 = 1.8.

D_{core}, μm	I_{max}, a.u.	DOF, λ	FWHM, λ	F, μm
2.0	7.97	0.78	0.37	0.02
1.9	5.06	1.06	0.35	0.19
1.8	3.26	1.69	0.62	0.31
1.7	4.47	1.49	0.48	0.17
1.6	5.24	1.86	0.53	0.24
1.5	**4.13**	**2.10**	**0.30**	**0.35**
1.4	3.10	2.61	0.63	0.65
1.3	3.34	2.22	0.62	0.56
1.2	4.01	1.82	0.58	0.48

From Table 2 we can see that the best design is represented by a two-layer cylinder with D_{core} = 1.5 μm. It can be noticed that the two-layered cylinder does not give such a high intensity in the focal spot as ordinary cylinder, but nevertheless, the depth of the formed focus is much higher than that is for the other presented models.

At last, we simulate similar cylinders, but for the shell made of polystyrene (n_2 = 1.59 [45]). The results are presented in Table 3.

From Table 3 we can see that a two-layered cylinder with a core diameter D_{core} = 1.9 μm allows the formation of the tight focus with the best parameters: high intensity and smallest FWHM and DOF.

To simplify the analysis of the obtained results we presented the dependence of focal spot characteristics in Fig. 2.

It can be seen from Fig. 2 that all shells lead to increasing of the focal length, FWHM and DOF. However, in each case of different materials for shell DOF (Fig. 2(b)) grows faster than FWHM (Fig. 2(c)). The maximum intensity is decreasing while using thick coatings (Fig. 2(a)).

Table 3 Parameters of the focal spot formed by the two-layered microcylinders with n_1 = 1.45 and n_2 = 1.59.

D_{core}, μm	I_{max}, a.u.	DOF, λ	FWHM, λ	F, μm
2.0	7.97	0.78	0.37	0.02
1.9	**10.43**	**0.56**	**0.17**	**0.00**
1.8	5.91	0.99	0.43	0.23
1.7	5.06	1.27	0.49	0.20
1.6	5.56	1.30	0.47	0.15
1.5	5.83	1.39	0.47	0.13
1.4	5.52	1.75	0.52	0.52
1.3	4.88	2.98	0.48	0.20
1.2	4.62	2.74	0.51	0.20

Distributions of intensity obtained while focusing of TE-polarized light by ordinary cylinder with n_1 = 1.45 and by two-layered cylinders with optimal ratio of core and shell are presented in Fig. 3.

It can be seen from the Fig. 3 that the nanojet for a two-layer cylinder has elongated shape in case of n_2 equal to 1.9 (Fig. 3(b)) and 1.8 (Fig. 3(c)). Moreover, it is formed at some distance from cylinder boundary. From the analysis of the Fig. 3(d) we can conclude that the dielectric shell with a refractive index which is a bit higher than the core refractive index allows to reduce the geometric dimensions of the focal spot and increase the intensity in focus.

Then we present series of numerical experiments for the same designs of microcylinders, but for TM-polarized plane wave as incident light. We briefly described the obtained results which are shown in Tables 4–6 and in Fig. 4.

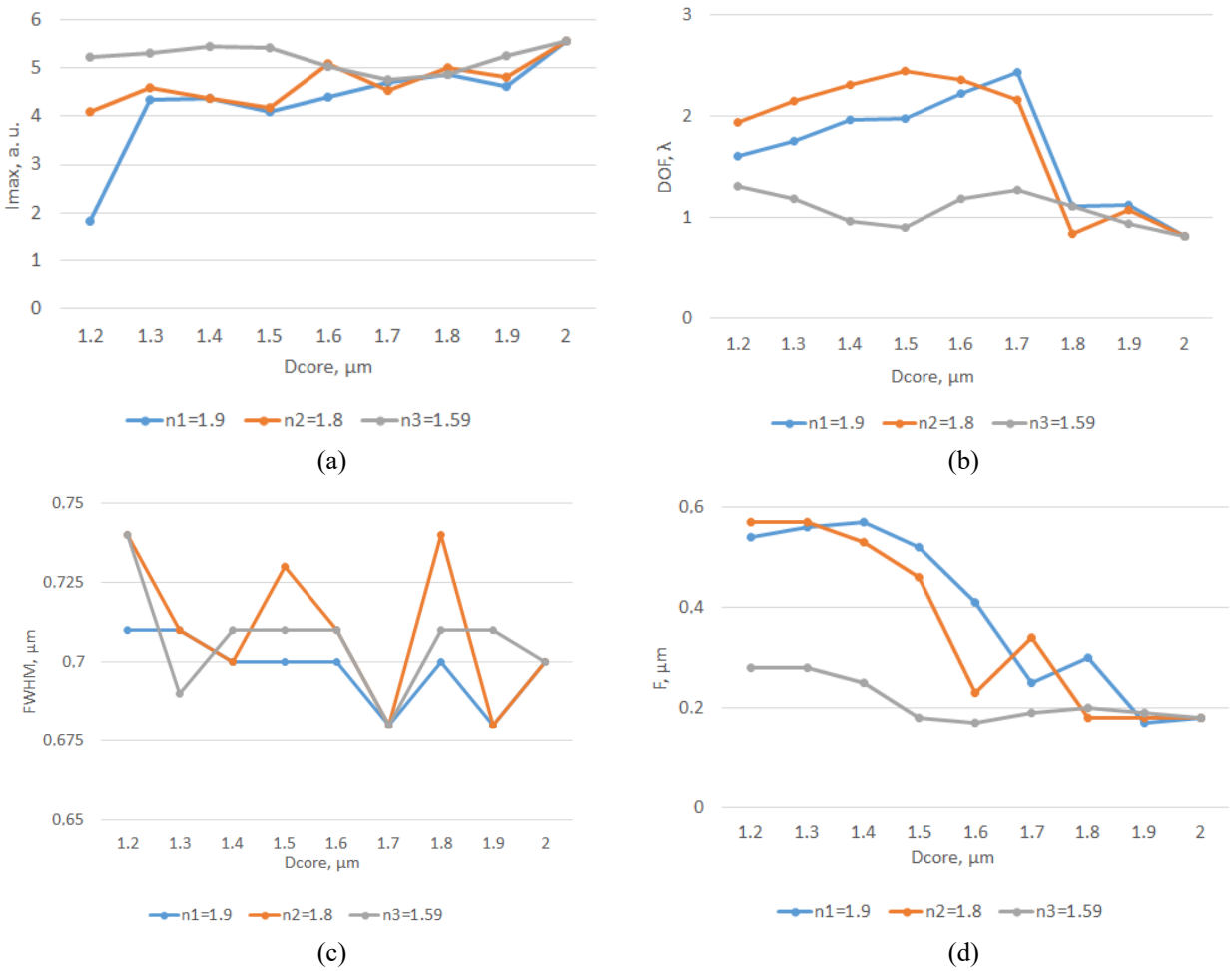


Fig.4 Dependence of the I_{max} (a), DOF (b), FWHM (c), F (d) on the core diameter for TM-wave.

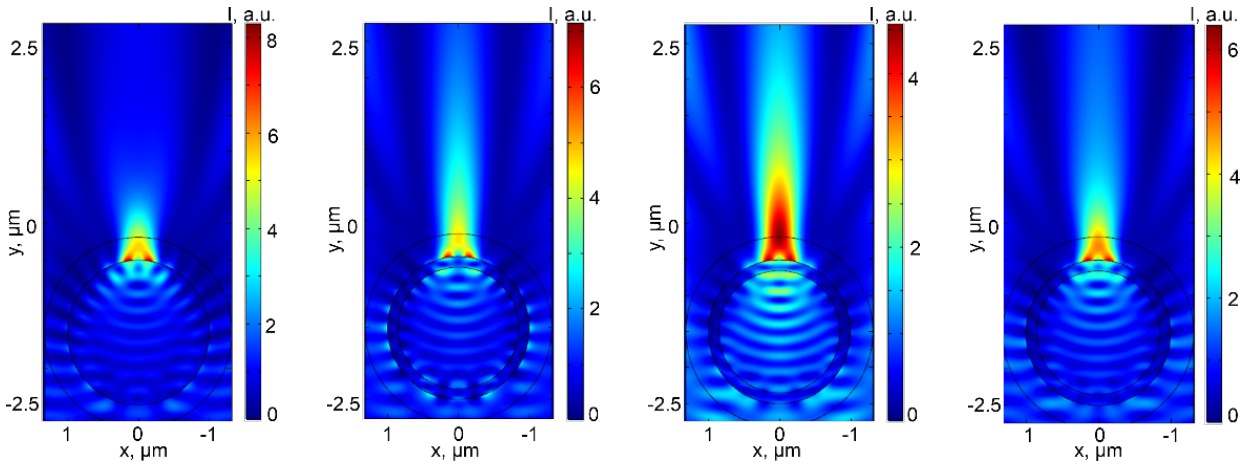


Fig. 5 The intensity distribution for ordinary microcylinder (a) and two-layered micrcylinders with n_2 =1.9 and D_{core} = 1.7 (b); n_2 =1.8 and D_{core} = 1.7 (c); n_2 =1.59 and D_{core} = 1.7 (d) illuminated by TM-wave.

It can be seen from Fig. 4 that the influence of shell on focusing process is not so significant as in the case of TE-polarization. Shells with high refractive indeces lead to decreasing of the maximum intensity. Fig. 4(b) shows that thick coatings of high refractive index lead to decreasing of the DOF and the optimal value of shell thickness is about 200–400 nm. It can be seen from Fig. 4(d) that all shells lead to increasing of the focal length. It should be mentioned that the polystyrene shell

does not significantly affects on all parameters of the nanojet.

Table 4 Parameters of the focal spot formed by the two-layered microcylinders with $n_1 = 1.45$ and $n_2 = 1.9$.

D_{core}, μm	I_{max}, a.u.	DOF, λ	FWHM, λ	F, μm
2.0	5.56	0.82	0.70	0.18
1.9	4.62	1.12	0.68	0.17
1.8	4.86	1.11	0.70	0.30
1.7	**4.70**	**2.43**	**0.68**	**0.25**
1.6	4.41	2.22	0.70	0.41
1.5	4.09	1.98	0.70	0.52
1.4	4.36	1.96	0.70	0.57
1.3	4.34	1.75	0.71	0.56
1.2	1.83	1.60	0.71	0.54

Table 5 Parameters of the focal spot formed by the two-layered microcylinders with $n_1 = 1.45$ and $n_2 = 1.8$.

D_{core}, μm	I_{max}, a.u.	DOF, λ	FWHM, λ	F, μm
2.0	5.56	0.82	0.70	0.18
1.9	4.82	1.07	0.68	0.18
1.8	5.00	0.84	0.74	0.18
1.7	**4.54**	**2.16**	**0.68**	**0.34**
1.6	5.08	2.36	0.71	0.23
1.5	4.19	2.44	0.73	0.46
1.4	4.36	2.31	0.70	0.53
1.3	4.60	2.15	0.71	0.57
1.2	4.09	1.94	0.74	0.57

It can be seen from the Table 4–6 and Fig. 4 that the two-layered microcylinders form a nanojet with a maximum DOF of 1.44λ, which is almost 3 times greater than the maximum intensity of the nanojet formed by a conventional dielectric cylinder. At the same time the FWHM was preserved and a decrease in the maximum intensity of the focal spot is about 20% of the maximum value. The distribution of intensity obtained while focusing of the TM-polarized light by the ordinary cylinder with $n_1 = 1.45$ and by two-layered cylinders with optimal ratio of the core and the shell is presented in Fig. 5.

Table 6 Parameters of the focal spot formed by the two-layered microcylinders with $n_1 = 1.45$ and $n_2 = 1.59$.

D_{core}, μm	I_{max}, a.u.	DOF, λ	FWHM, λ	F, μm
2.0	5.56	0.82	0.70	0.18
1.9	5.26	0.94	0.71	0.19
1.8	4.86	1.11	0.71	0.20
1.7	**4.76**	**1.27**	**0.68**	**0.19**
1.6	5.03	1.18	0.71	0.17
1.5	5.41	0.90	0.71	0.18
1.4	5.46	0.96	0.71	0.25
1.3	5.30	1.19	0.69	0.28
1.2	5.24	1.31	0.74	0.28

It can be seen from Fig. 5 that using a shell makes it possible to form a single peak, in contrast to using a uniform microcylinder with a refractive index of 1.45, which forms a focal spot with two aligned peaks. In addition, nanojets obtainedin the case of using a two-layered microcylinder has a more elongated shape. Moreover, they are located at a considerable distance from the boundary of the cylinder.

3.2 Comparison of numerical results with FDTD-method

In this section, the results of numerical modeling for cylinders with a similar design are shown. But in this case FDTD-method implemented in the FullWAVE software package was used for numerical calculations. The results of light focusing by microcylinders with the best designs are presented in Table 7.

Table 7 Parameters of the focal spot formed by ordinary microcylinders and two-layered microcylinders with the best designs.

Polarization	n_1	n_2	D_{core}, μm	I_{max}, a.u.	DOF, λ	FWHM, λ	F, μm
TE	1.45	-	2.0	8.18	0.73	0.32	0.00
	1.45	1.9	1.6	5.03	1.13	0.33	0.60
	1.45	1.8	1.5	4.17	2.02	0.51	0.39
	1.45	1.59	1.9	11.12	0.51	0.25	0.00
TM	1.45	-	2.0	5.53	0.85	0.70	0.15
	1.45	1.9	1.7	5.05	1.58	0.70	0.31
	1.45	1.8	1.7	4.89	0.74	0.44	0.48
	1.45	1.59	1.7	4.63	1.36	0.45	0.64

Table 7 shows that the results obtained using FullWAVE based on FDTD method are in good agreement with the results of COMSOL Multiphysics based on FEM.

The obtained results have a big potential in different biomedicine applications [48–50]. In particular, one of the most important stages of sample preparation in biomedical research is cell separation [48]. It is necessary to purify the target cell population and minimize intercellular interactions prior to biomedical analysis. An optical tweezer or an optical scalpel which is laser radiation focused into a nanojet can be used to separate cells [51]. The fluorescence-based optical detection and imaging technologies are widely used in biomedicine [49]. However, low fluorescence intensity decreases the detection sensitivity and the image brightness. Photonic nanojets can concentrate an incident light in the subwavelength rangeforming a narrow high-energy beam and, thus, increase energy density and enhance fluorescence [52]. The extensive results on the nanofabrication of plasmonic structures stimulated the usage of photonic nanojets for patterning substrates suitable for surface-enhanced spectroscopy, specifically, surface-enhanced Raman scattering (SERS) and surface-enhanced infrared absorption (SEIRA) [50].

4 Conclusions

In this paper, the process of laser light focusing by two-layer dielectric microcylinders of the circular cross-section is investigated. For numerical modeling COMSOL Multiphysics based on the finite element method (FEM) was chosen. Obtained results were verified by FullWAVE based on the finite difference time domain method (FDTD method). We investigated the effect of cladding on the focusing of TE- and TM-polarized laser light with a wavelength of 633 nm. The refractive index of the core was fixed at 1.45 (fused silica glass [45]), while the different refractive indices for the cladding were taken into account: 1.9 (SiN [46])), 1.8 (titanium oxide-organic polymer [47]), and 1.59 (polystyrene [45]). It has been shown that claddings with a higher refractive index than the core refractive index make it possible to increase the depth of the focus and shift the focus away from the cylinder boundary. For example, the design with a shell refractive index of $n_2 = 1.8$ can increase the depth of the field 3 times for both TE and TM waves. At the same time, if the difference between the refractive indices of the core and the cladding is not too large a two-layer microcylinder can focus the TE-wave in a narrow focal spot the spatial parameters of which are extremely small. For example, a two-layer microcylinder with the core and the shell refractive indices of 1.45 and 1.59, respectively, formed a more compact focal spot (FWHM = 0.32λ, DOF = 0.16λ) with an intensity (I_{max} = 11.12 a.u.) 1.4 times higher than the intensity of the focus formed by an ordinary cylinder with a refractive index n = 1.45. The proposed designs of two-layer microcylinders are easier to manufacture than designs presented in Refs. [31, 53].

The obtained results can find application in various fields such as nanosensorics [54], nanolithography [55], and microscopy [56], and biomedicine [48–50]. As it was mentioned before, the investigation of the photonic nanojet formation can be useful for successful in all stages of biofluids and biosamples [57] study:from preparation [51] to imaging [52].

Disclosures

All authors declare that there is no conflict of interests in this paper.

Acknowledgments

This work was supported by the Russian Foundation for Basic Research RFBR (Grant No. 18-29-20003) in the part of TE-polarization, the Russian Science Foundation (Grant No. 18-19-00595) in the part of TM-polarization, and the Ministry of Science and Higher Education in the framework of works on the State task of the Federal Research Center "Crystallography and Photonics" RAS in the parts "Introduction" and "Conclusion".

References

1. S. Zhou, "Effects of light polarization in photonic nanojet," Optical and Quantum Electronics 51, 112 (2019).
2. V. V. Kotlyar, S. S. Stafeev, and A. A. Kovalev, "Sharp focusing of a light field with polarization and phase singularities of an arbitrary order," Computer Optics 43(3), 337–346 (2019).
3. A. Darafsheh, "Photonic nanojets and their applications," Journal of Physics: Photonics 3(2), 022001 (2021).
4. J. Zhu, L. L. Goddard, "All-dielectric concentration of electromagnetic fields at the nanoscale: the role of photonic nanojets," Nanoscale Advances 1, 4615–4643 (2019).
5. I. V. Minin, C.-Y. Liu, Y. E. Geints, and O. V. Minin, "Recent Advances in Integrated Photonic Jet-Based Photonics," Photonics 7(2), 41 (2020).
6. X. Chen, M. E. Kandel, and G. Popescu, "Spatial light interference microscopy: principle and applications to biomedicine," Advances in Optics and Photonics 13(2), 353–425 (2021).
7. S. Gao, K. Meng, Z. Yang, H. Liu, F. Wang, L. Sun, and T. Chen, "The Probe-combined Microspheres Applied in Biomedical Field for Super-resolution Imagings and Micromanipulations," In 4th Asia-Pacific Conference on Intelligent Robot Systems (ACIRS), 155–158 (2019).
8. A. Shakhov, A. Astafiev, and V. Nadtochenko, "Microparticle manipulation using femtosecond photonic nanojet-assisted laser cavitation," Optics Letters 43(8), 1858 (2018).

9. S. Surdo, M. Duocastella, and A. Diaspro, "Nanopatterning with Photonic Nanojets: Review and Perspectives in Biomedical Research," Micromachines 12(3), 256 (2021).
10. D. Lu, M. Pedroni, L. Labrador-Paez, M. I. Marques, D. Jaque, and P. Haro-Gonzalez, "Nanojet Trapping of a Single Sub-10 nm Upconverting Nanoparticle in the Full Liquid Water Temperature Range," Nano Micro Small 17(7), 2006764 (2021).
11. R. Ali, F. A. Pinheiro, R. Dutra, F. Rosa, and P. A. M. Neto, "Enantioselective manipulation of single chiral nanoparticles using optical tweezers," Nanoscale 12(8), 5031–5037 (2020).
12. X. Shan, F. Wang, D. Wang, S. Wen, C. Chen, X. Di, P. Nie, J. Liao, Y. Liu, L. Ding, P. J. Reece, and D. Jin, "Optical tweezers beyond refractive index mismatch using highly doped upconversion nanoparticles," Nature Nanotechnology 16, 531–537 (2021).
13. J. L. Killian, F. Ye, and M. D. Wang, "Optical Tweezers: A Force to Be Reckoned With," Cell 175(6), 1445–1448 (2018).
14. W. Zhang, H. Lei, "Fluorescence enhancement based on cooperative effects of a photonic nanojet and plasmon resonance," Nanoscale 12(12), 6596–6602 (2020).
15. O. V. Polschikova, A. S. Machikhin, A. G. Ramazanova, I. A. Bratchenko, V. E. Pozhar, I. V. Danilycheva, O. R. Katunina, and M. V. Danilychev, "An Acousto-Optic Hyperspectral Unit for Histological Study of Microscopic Objects," Optics and Spectroscopy 125(6), 1074–1080 (2018).
16. L. A. Bratchenko, I. A. Bratchenko, Y A. Khristoforova, D. N. Artemyev, D. Y. Konovalova, P. A. Lebedev, and V. P. Zakharov, "Raman spectroscopy of human skin for kidney failure detection," Journal of Biophotonics 14(6), e202000360 (2020).
17. Z. Zhen, Y. Huang, Y. Feng, Y. Shen, and Z. Li, "An ultranarrow photonic nanojet formed by an engineered two-layer microcylinder of high refractive-index materials," Optics Express 27(6), 9178–9188 (2019).
18. A. Darafsheh, D. Bollinger "Systematic study of the characteristics of the photonic nanojets formed by dielectric microcylinders," Optics Communications 402, 270–275 (2017).
19. A. Darafsheh, D. Bollinger, "Photonic nanojet properties of dielectric microcylinders," Proceedings of SPIE 10106, 101061U (2017).
20. Y. E. Geints, A. A. Zemlyanov, I. V. Minin, and O. V. Minin, "Overcoming refractive index limit of mesoscale light focusing by means of specular-reflection photonic nanojet," Optics Letters 45(14), 3885–3888 (2020).
21. S. Zhou, T. Zhou, "An ultra-narrow photonic nanojet generated from a high refractive-index micro-flatended cylinder," Applied Physics Express 13, 042010 (2020).
22. A. A. Savelyeva, E. S. Kozlova, "Simulation of laser light focusing with two-layer dielectric microcylinders," Computer Optics 45(2), 208–213 (2021).
23. V. D. Zaitsev, S. S. Stafeev, "The photonic nanojets formation by two-dimensional microprisms," Computer Optics 44(6), 909–916 (2020).
24. A. Abramov, Y. Yue, M. Wang, Z. Wang, and Y. Xu, "Numerical Modeling of Photonic Jet behind Triangular Prism," Asian Journal of Research and Reviews in Physics 4(1), AJR2P.63969 (2021).
25. S. Zhou, K. Li, and Y. Wang, "Tunable photonic nanojets from a micro-cylinder with a dielectric nano-layer," Optik 225, 165878 (2021).
26. Y. Cao, Z. Liu, and O. V. Minin, "Deep Subwavelength-Scale Light Focusing and Confinement in Nanohole-Structured Mesoscale Dielectric Spheres," Nanomaterials 9(2), 186 (2019).
27. D. Grojo, N. Sandeau, L. Boarino, C. Constantinescu, N. De Leo, M. Laus, and K. Sparnacci, "Bessel-like photonic nanojets from core-shell sub-wavelength spheres," Optics Letters 39(13), 3989 (2014).
28. A. A. Savelyeva, E. S. Kozlova, "Simulation of laser light focusing by a dielectric nanocylinder with gold core," Journal of Physics: Conference Series 1368, 022030 (2019).
29. C.-Y. Liu, K.-L. Hsiao, "Direct imaging of optimal photonic nanojets from core-shell microcylinders," Optics Letters 40(22), 5303–5306 (2015).
30. A. A. Savelyeva, E. S. Kozlova, "Simulation of light focusing by a dielectric microcylinder with a metal film and gap on shadow side," Journal of Physics: Conference Series 1745, 012010, (2021).
31. Y. Huang, Z. Zhen, Y. Shen, C. Min, and G. Veronis, "Optimization of photonic nanojets generated by multilayer microcylinders with a genetic algorithm," Optics express 27(2), 1310–1325 (2019).
32. A. A. Savelyeva, E. S. Kozlova, "Simulation of laser light focusing by two-layered dielectric cylinders," In 22nd International Conference on Transparent Optical Networks, 19–23 July 2020, 1–4 (2020).
33. M. N. O. Sadiku, "A simple introduction to finite element analysis of electromagnetic problems," IEEE Transactions on Education 32(2), 85–93 (1989).
34. D. W. Pepper, J. C. Heinrich, The Finite Element Method: Basic Concepts and Aplications with MATLAB, MAPLE, and COMSOL, 3rd ed., CRC Press, Boca Raton, USA (2017).
35. S. Singh, R. S. Kaler, "Performance analysis of evanescent wave absorption plasmonic optical sensor with COMSOL FEM method simulation," Procedia Computer Science 125, 376–381 (2018).

36. V. D. Zaitsev, S. S. Stafeev, "Photonic Jets Arrays Produced by Triangular Dielectric Prisms for Mid-IR Imaging," In 2019 PhotonIcs & Electromagnetics Research Symposium – Spring (PIERS-Spring), 17–20 June 2019, 2610–2614 (2019).
37. E. S. Kozlova, V. V. Kotlyar, and S. A. Degtyarev, "Simulation of resonance focusing of a picosecond pulse by a dielectric microcylinder," Computer Optics 39(1), 45–51 (2015).
38. M. A. Born, E. Wolf, Principles of optics Electromagnetic Theory of Propagation, Interference, and Diffraction of Light, Cambridge University Press, London (1999).
39. K. S. Yee, "Numerical Solution of Initial Boundary Value Problems Involving Maxwell's Equations in Isotropic Media," In IEEE Transactions on Antennas and Propagation 14(3), 302–307 (1966).
40. S. D. Gedney, "Introduction to the Finite-Difference Time-Domain (FDTD) Method for Electromagnetics," Synthesis Lectures on Computational Electromagnetics 6(1), 1–250 (2011).
41. X. Guo, Y. Ding, X. Chen, Y. Duan, and X. Ni, "Molding free-space light with guided wave–driven metasurfaces," Science Advances 6(29), eabb4142 (2021).
42. A. G. Nalimov, "Energy flux of a vortex field focused using a secant gradient lens," Computer Optics 44(5), 707–711 (2020).
43. E. S. Kozlova, S. S. Stafeev, S. A. Fomchenkov, V. V. Podlipnov, and V. V. Kotlyar, "Laser Light Focusing by Aluminium Zone Plate," In 22nd International Conference on Transparent Optical Networks, 1–4 (2020).
44. S. Piltyay, A. Bulashenko, Y. Herhil, and O. Bulashenko, "FDTD and FEM Simulation of Microwave Waveguide Polarizers," In IEEE 2nd International Conference on Advanced Trends in Information Theory, 357–363 (2020).
45. J. F. Shackelford, Introduction to Materials Science for Engineers, 5th ed., McGraw-Hill, New York (2000).
46. H. Nagel, A. G. Aberle, and R. Hezel, "Optimised antireflection coatings for planar silicon solar cells using remote PECVD silicon nitride and porous silicon dioxide," Progress in Photovoltaics: Research and Applications 7(4), 245–260 (1999).
47. T. D. Flaim, Y. Wang, and R. Mercado, "High-refractive-index polymer coatings for optoelectronics applications," Advances in Optical Thin Films 5250, 423–434 (2004).
48. N. Liu, C. Petchakup, H. M. Tay, K. H. H. Li, and H. W. Hou, "Spiral Inertial Microfluidics for Cell Separation and Biomedical Applications," Cell Culture Techniques, 99–150 (2019).
49. W. Zhang, H. Lei, "Fluorescence enhancement based on cooperative effects of a photonic nanojet and plasmon resonance," Nanoscale 12(12), 6596–6602 (2020).
50. S. Surdo, M. Duocastella and A. Diaspro, "Nanopatterning with Photonic Nanojets: Review and Perspectives in Biomedical Research," Micromachines 12(3), 256 (2021).
51. A. A. R. Neves, "Photonic nanojets in optical tweezers. Journal of Quantitative Spectroscopy and Radiative Transfer," Journal of Quantitative Spectroscopy and Radiative Transfer 162, 122–132 (2015).
52. W. Liu, X. Li, Y. Song, C. Zhang, X. Han, H. Long, B. Wang, K. Wang, and P. Lu, "Cooperative Enhancement of Two-Photon-Absorption-Induced Photoluminescence from a 2D Perovskite-Microsphere Hybrid Dielectric Structure," Advanced Functional Materials 28(26), 1707550 (2018).
53. H. Zhang, "Enhanced subwavelength photonic nanojet focusing via a graded-index round-head microcylinder," Optik 203, 163973 (2020).
54. S. Cheng, X. Zhang, W. Ma, and S. Tao, "Detecting a Zeptogram of Pyridine with a Hybrid Plasmonic–Photonic Nanosensor," ACS Sens 4(3), 586–594 (2019).
55. J. Wei, K. Zhang, T. Wei, Y. Wang, Y. Wu, and M. Xiao, "High-speed maskless nanolithography with visible light based on photothermal localization," Scientific Reports 7, 43892 (2017).
56. R. Tenne, U. Rossman, B. Rephael, Y. Israel, A. Krupinski-Ptaszek, R. Lapkiewicz, Y. Silberberg, and D. Oron, "Super-resolution enhancement by quantum image scanning microscopy," Nature Photonics 13, 116–122 (2019).
57. L. A. Bratchenko, I. A. Bratchenko, A. A. Lykina, M. V. Komarova, D. N. Artemyev, O. O. Myakinin, A. A. Moryatov, I. L. Davydkin, S. V. Kozlov, and V. P. Zakharov, "Comparative study of multivariative analysis methods of blood Raman spectra classification," Journal of Raman Spectroscopy 51(2), 279–292 (2019).

Hyperspectral Camera – Attachment for Microscopy

Mohammed M. Hamza[1], Ali Hamandi[1], Andrey R. Makarov[1,2*], Vladimir V. Podlipnov[1,2], and Roman V. Skidanov[1,2]

[1] Samara National Research University, 34 Moskovskoe Shosse, Samara 443086, Russian Federation
[2] IPSI RAS – branch of the FSRC "Crystallography and Photonics" RAS, 151 Molodogvardejskaya str., Samara 443001, Russian Federation

*** e-mail:** andre_makar@bk.ru

Abstract. The paper presents a microscope equipped with a hyperspectral ocular nozzle with a phase diffraction grating, which is used as a dispersing element. The spectral range of the device is 400–1000 nm, with the spectral resolution of 5 nm. The paper describes a microscope software that is used to solve problems of spectral analysis. © 2021 Journal of Biomedical Photonics & Engineering.

Keywords: microscopy; hyperspectral imaging; hyperspectral analysis.

Paper #3429 received 24 May 2021; revised manuscript received 25 Sep 2021; accepted for publication 25 Sep 2021; published online 30 Sep 2021. doi: 10.18287/JBPE21.07.030405.

1 Introduction

Hyperspectral equipment that can distinguish a large number of spectral channels, in contrast to conventional three-color imaging, when using hyperspectral image processing, allows you to see subtle color differences in the visible range of optical radiation, as well as wavelengths invisible to the human eye in the near-infrared range [1]. This ability makes it possible to distinguish a number of chemical compounds of the underlying surface in remote sensing of the Earth, and is also increasingly used in biology and medicine [2]. In addition to the classical search signatures, in biology and medicine, a number of compounds with the use of illumination of certain wavelengths can cause the effect of photoluminescence, fluorescence, Raman scattering, etc., which allows you to use the hyperspectral equipment in criminology [3], materials science [4], mineralogy [5]. Such studies can be carried out only in the laboratory, and the use of a combination of microscopy and hyperspectral equipment allows you to see the smallest particles that cannot be seen by the eye [6].

A microscope with hyperspectral imaging can use narrow-band radiation of an object, or radiation transmitted through an optical monochromator [7]. Hyperspectral imaging systems based on acousto-optic modulators are known [8]. Most often, hyperspectrometers use an optical scheme of the scanning type, similar to that described in Ref. [9]. Using a microscope-spectrometer, it is possible to obtain the spectrum of individual pixels in the wavelength range from 400 nm to 1000 nm with a spectral resolution of 5 nm [10–11], depending on the dispersing element used and the resolution of the recording matrix.

We analyze well-known microscopes equipped with spectrum recording systems, and some of their shortcomings become obvious. One of them is the complexity and high cost of the optical or electronic part of the devices. For example, the LOMO MSFU-K microscope-spectrophotometer uses a photoelectron multiplier PMF R928 from Hamamatsu (Japan). Many devices do not allow you to get spectral data in each individual pixel of the image. Most instruments do not have an option of selecting a microscope. The complex can only be installed on certain microscopes.

In this regard, in this paper, the task is to develop and study a hyperspectrometer adapted to work as part of a microscope in the form of an ocular nozzle. Scanning can be carried out by moving the movable table of the microscope. This concept makes it possible to equip almost any microscope for biological research with a hyperspectral imaging system.

2 Materials and Methods

2.1 Optical scheme of a hyperspectral camera to a microscope

The optical unit of a hyperspectral camera for a microscope is made according to a fairly well-known scheme of a slit hyperspectrometer based on a grating dispersion element. Most schemes have a prism or lattice dispersion element. Since the grid has a more compact size, it was decided to use it. A standard microscope lens with a magnification of 10×, 20×, 40×, 100× is used as an input lens. This set of magnifications is most often used in biomedical researches [12–13]. The image from these lenses is built on a slit aperture having a slit width of about

10 µm. Next, a telescopic system based on two lenses builds an image of the gap on the matrix. A binary lattice with a period of 6 µm is installed inside the telescope. Such grating provides about 250 channels in the focal plane in the spectral range of 400–1000 nm.

The design elements of the hyperspectral nozzle were developed according to the optical scheme (see Fig. 1) using three-dimensional modeling of 3D printing parts made of plastic on a 3D lapper.

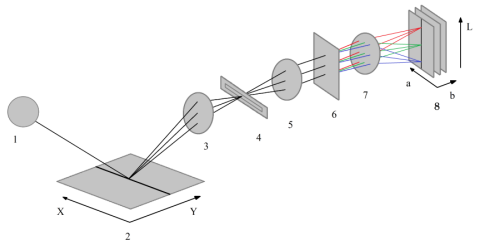


Fig. 1 Optical scheme of a hyperspectral measuring device for a microscope.

An optical hyperspectrometer consists of the following elements: 1) light source; 2) motorized table; 3) focusing lens; 4) entrance slit; 5) collimator; 6) dispersion grid; 7) focusing lens; 8) optical sensor, L – wavelength; a, b – 2D detector arrays.

For illumination, both the built-in halogen lamp of the microscope and the external one with an upper position can be used. In this case, the generated spectrum on the sensor is recorded as the transmission spectrum and the reflection spectrum, respectively.

2.2 Hyperspectral survey control system as part of a microscope

The fact that the camera is based on slit scanning will be used as the basis of the shooting control system for obtaining hyperspectral images (hypercubes). In our case, the hyperspectral camera remains stationary, while relative to it, the movement is carried out by scanning a sample located on a movable microscope table. The microscope has precise mechanical movement elements. Usually, the operator manually rotates these handles and visually observes the area on the slide table. For automated control of these movements, it is possible to install a stepper motor. Thus, with the help of a special control system, it is possible to install the step and speed of movement from the control unit.

The control unit of the complex is based on a single-board microcomputer with software for shooting and an optical sensor of the camera synchronized with the shooting and a motion control system for the scanning table. The control is carried out by sending control signals to the stepper motor driver. The camera registers the signal during the time allotted for the accumulation of light by the optical sensor, at the end of which the next signal for movement is formed. At the end of the movement, the next frame begins to be shot synchronously. The time of accumulation of the signal from the matrix, the number of shooting frames, etc. shooting parameters are set using the developed user interface. The structure of the complex is shown in Fig. 2. In order to control the shooting, a compact, sufficiently powerful computer is needed.

The complex uses a Raspberry Pi 4 microcomputer due to the large number of GPIO pins, a large set of USB and HDMI interfaces, the presence of Wi-Fi and Bluetooth. The manufacturer is “Raspberry Pi Foundation”, England.

Also, the A3967SLB stepper motor driver (Allegro MicroSystems, USA) is used in the complex. The complex uses a monochrome camera “Basler acA 1920–40 um” (BASLER Fashion GmbH, Germany).

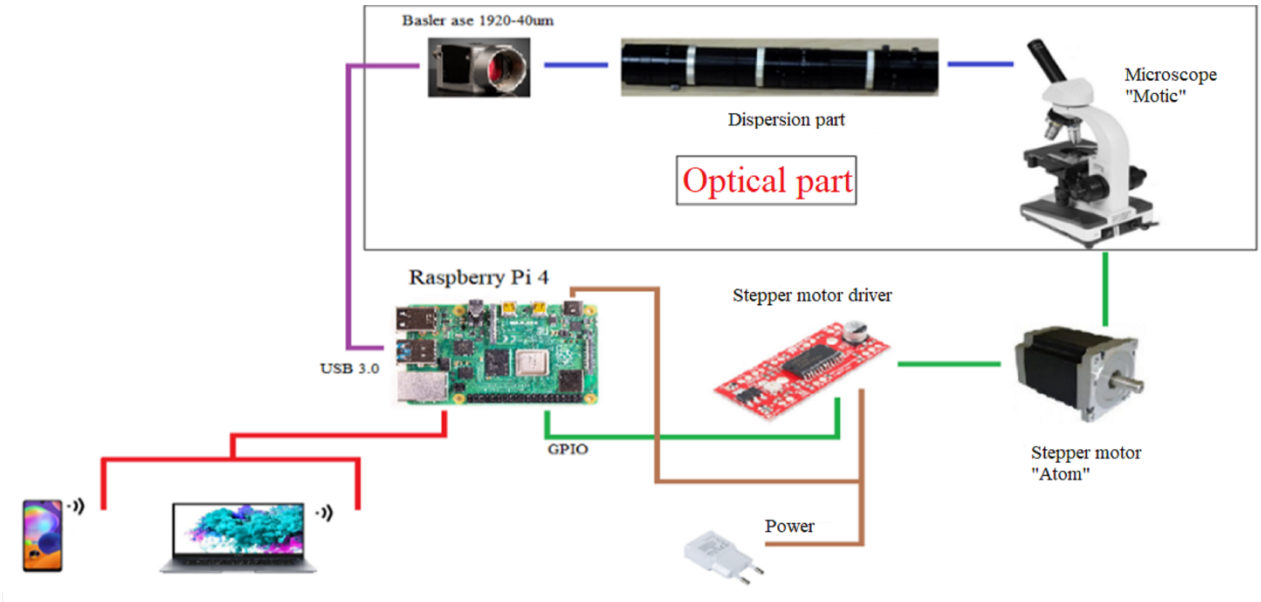


Fig. 2 Block diagram of the software and hardware complex.

The monochrome camera was chosen because of its greater light sensitivity and it can capture a larger range, unlike a color camera.

The ATOM stepper motor (ATOM, Russia) was chosen:

1) Angular pitch, deg –1.8.

2) The error of the angular step, deg ±5% (full step, without load).

The information collected in this way is processed by special software for recognizing objects with similar spectral characteristics.

A stepper motor is attached to the movable microscope substrate. The stepper motor is connected to the movable table of the microscope through a gearbox consisting of two gears. Gear ratio equals to 3. The image of the engine design is shown in Fig. 3.



(a)



(b)

Fig. 3 (a) The image shows a microscope, (b) motor design for moving the microscope table.

The stepper motor driver is controlled by a Raspberry Pi 4 single-board computer via GPIO ports [14].

The Python program controls the signals “1” and “0” on the GPIO ports using the python library RPi.GPIO.

The presented complex uses the stepper motor driver “A3967LBT”.

The signals are fed to the inputs of the A3967LBT driver and, thus, the stepper motor is controlled [15]. The presented stepper motor driver allows you to work with step crushing modes in the range from full-step to 1/8 step, which on the microscope under study provides an accuracy of movement from 32.4 μm per step in full-step mode, to 4.05 μm in 1/8 step mode.

The Basler camera is connected to the computer via a USB 3.0 port. The camera parameters were changed using the Python SDK using the pypylon library. Shooting settings: shutter speed, if using a color camera, the white balance value [16].

To set the settings for shooting, you need an interface (Fig. 4). To create it, we used the PyQt5 program.

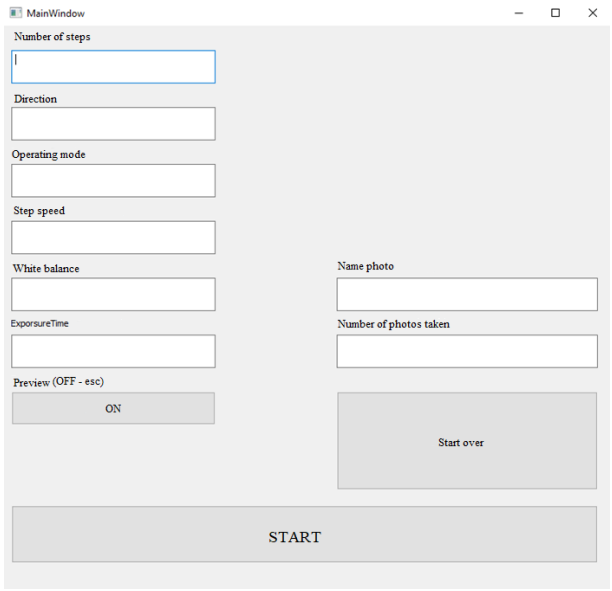


Fig. 4 Interface for managing shooting parameters.

The “ON Preview” button allows you to see what is in real time on the microscope substrate.

This may be necessary to adjust the focus. The “Start over” button clears the fields. The “START” button starts shooting.

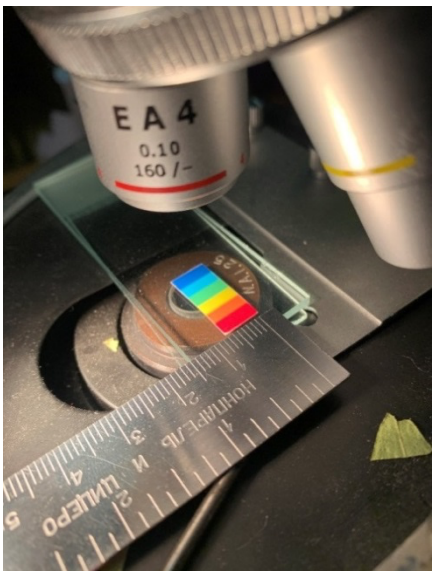
Shooting can be controlled remotely via Wi-Fi, via a separate computer or smartphone using the VNC viewer remote access program.

3 Results and Discussion

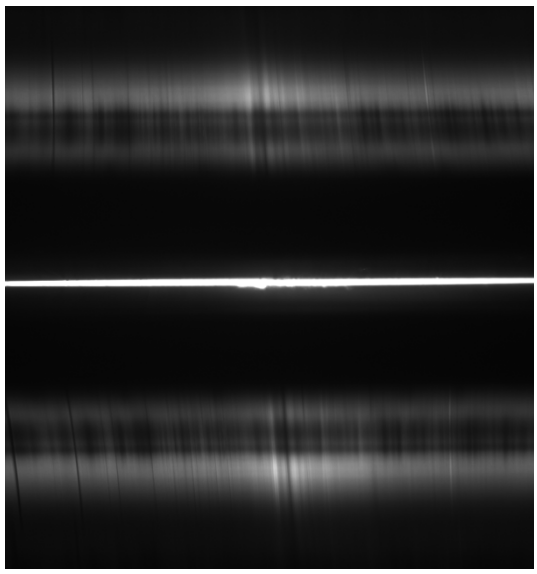
We tested the resulting scanning and hyperspectral shooting control system, carried out the necessary tests, calibrations, scanning speed settings, exposure, etc. We also determined the optical characteristics of the hyperspectral attachment to the microscope. A hyperspectral image (hypercube) is obtained by assembling frames from a sequence taken at each step of the stepper motor using specially developed software.

When testing the complex (see Fig. 5), a multi-colored paper printed on an inkjet printer was photographed (see Fig. 5a).

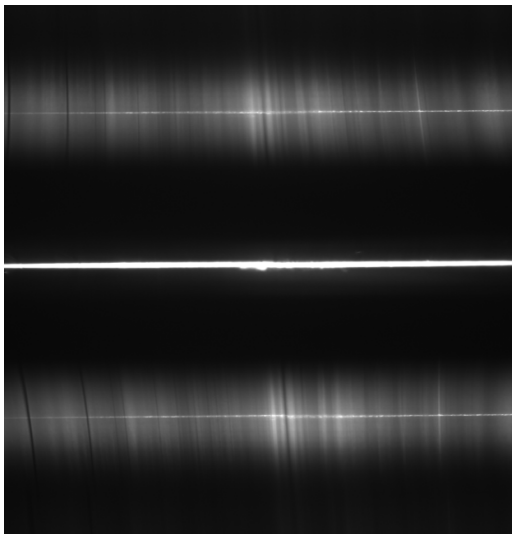
The image of a single frame fixed on the CCD matrix of the hyperspectral camera, illuminated by a halogen lamp (Fig. 5b).



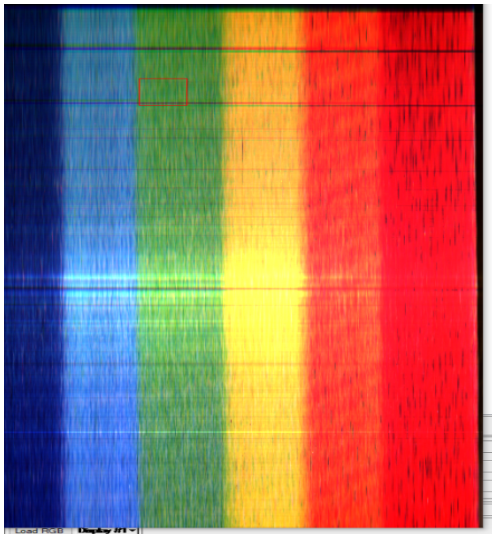
(a)



(b)



(c)



(d)

Fig. 5 (a) An object, (b) the image of a single frame fixed on the CCD matrix of the hyperspectral camera attachment of the microscope, (c) spectrum image on a hyperspectrometer camera with additional illumination by a laser with a wavelength of 532 nm, (d) an RGB image of colored paper synthesized from hypercube channels in the ENVI program The dimensions of the shooting area are 4.5 mm wide and 14 mm long.

In order to carry out the correct color synthesis for this hyperspectral camera, laser calibration was carried out with a wavelength of 532 nm. The view of the image of the spectral decomposition of the image in the slot from the object that is additionally illuminated by the laser is shown in Fig. 5c. From this image, it is also possible to estimate the spectral resolution of the hyperspectrometer, which, as can be seen, allows distinguishing about 120 spectral channels in the range of 400–1000 nm. In this case, it is easy to get that the spectral resolution in this case becomes about 5 nm.

The spectrum data was obtained and converted into a hypercube using special software. The three layers of the hypercube, which are responsible for the blue, green, and red components, were used to create the RGB image (see Fig. 5d).

Some “stripes” were skipped due to the 1/2 shooting mode, and therefore the proportions of the length and width of the image in Fig. 5d are equal to each other. You can set a smaller step (shooting mode 1/8), then all the proportions will be observed.

We can observe the spectrum at each point of this image. An example of the spectrum of pixels from the green area of colored paper (Fig. 5b) “rainbow” is shown in Fig. 6.

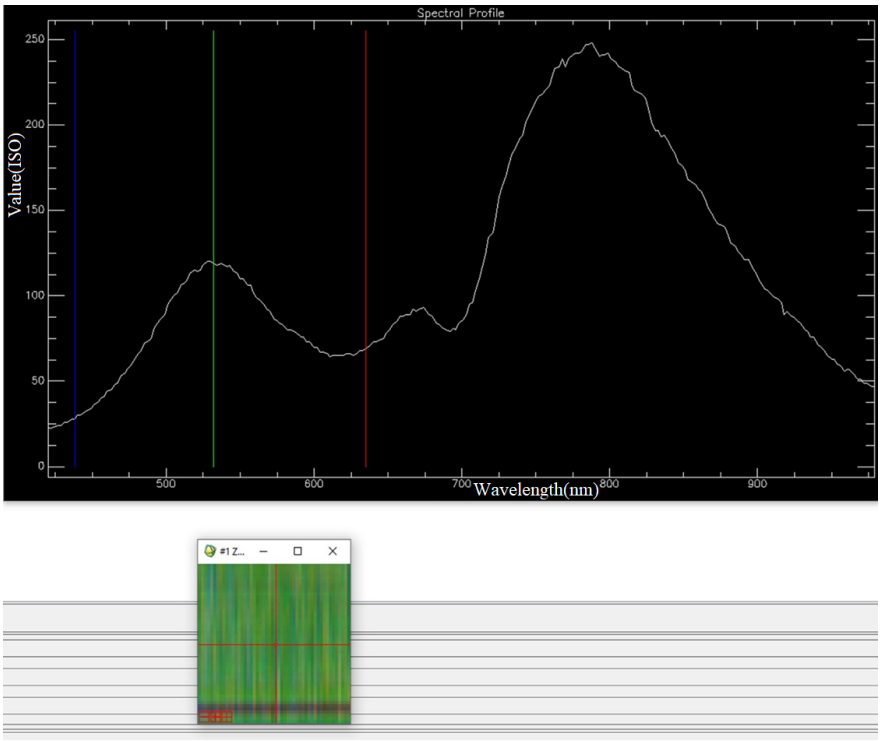


Fig. 6 Spectral analysis in the "ENVI" program.

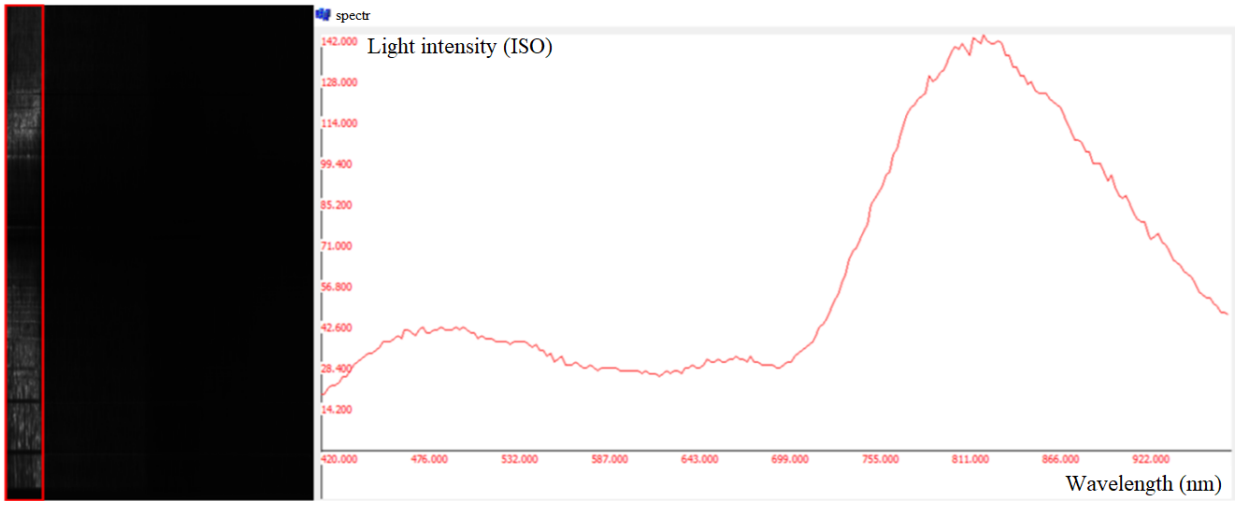


Fig. 7 The result of the classification of the object in the image. The dimensions of the shooting area are 4.5 mm wide and 14 mm long. Some "stripes" were skipped due to the 1/2 shooting mode, and therefore the proportions of the length and width of the image in Fig. 5d are equal to each other. You can set a smaller step (shooting mode 1/8), then all the proportions will be observed.

Fig. 6 shows the spectral analysis of the "rainbow" image – the green pixel is selected.

In this case, the ENVI program was chosen for spectral analysis. ENVI is a software for image processing and analysis. It is used by image analysts, GIS specialists and scientists to extract timely, reliable and accurate information from geospatial images.

The developer of the ENVI program "L3 Harris Technologies" is an American technology company, a defense contractor and an information technology service provider.

For example, we also carried out the classification of color bands with threshold processing by the well-known Euclidean distance method [17]. The result of selecting one strip from the image of colored paper (Fig. 5) is shown in Fig. 7.

For this purpose, a special software has been developed, with the help of which it is possible to quickly find objects of interest to research with a spectrum similar to the spectrum specified as the search standard. The spectrum can be loaded as a file or specified as an object in the image.

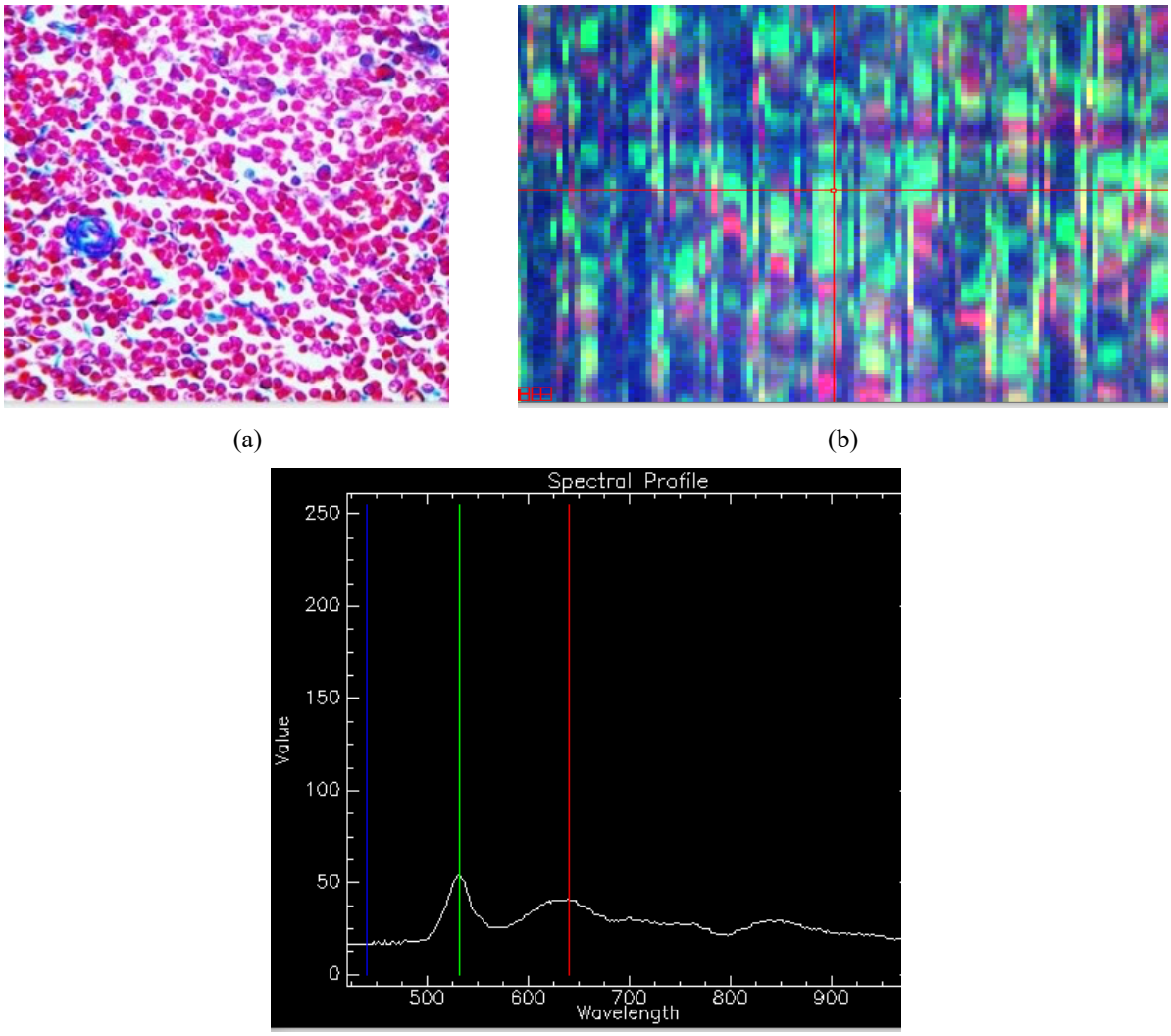


Fig. 8 An example of a hyperspectral image of a biological histology sample of a rat's spleen stained with hematoxylin-eosin: (a) an image of a sample of a rat spleen taken with a conventional camera through a microscope, (b) an image of a sample of a rat's spleen made by a hardware and software complex, (c) the spectrum of the selected point (wavelenght in nm).

We also obtained medical hyperspectral images of histological specimens for studying of rat's spleen from a set of micropreparations according to the catalog [18], produced by the company "Retinoids", produced in compliance with ethical requirements and international recommendations for conducting biomedical research using animals. An example of an image obtained in a microscope with an 40× magnification and its color-synthesized image is shown in Fig. 8.

Fig. 8a shows an image of a histological sample using an 10× lens and a ToupCam U3CMOS05100KPA microscope camera. The field of view is 0.9 × 0.9 mm.

Fig. 8b shows the image obtained by scanning in the 1/8 step mode, the size of the scanning area is 0.4 mm high and 1.2 mm wide. The proportions of the image are not observed due to the limited scanning step. Fig. 8c also shows an example of the spectrum in the cross-hair marker (Fig. 8b) area in the image. The hyperspectral additive for the microscope gives an additional magnification of about 2×.

In the future, we plan to continue our research to obtain methods for classifying objects in the image of medical samples. In this work, the task of determining the accuracy of the classification of anomalies associated with diseases was not set. To conduct this kind of research, we plan to conduct a survey of a large set of various biological preparations. In this work, the task of determining the accuracy of the classification of anomalies associated with diseases was not set. To conduct this kind of research, we plan to conduct a survey of a large set of various biological preparations. Previously, studies of hyperspectral imaging were conducted in Refs. [19, 20] to determine the types of human skin neoplasms. These studies have shown a fairly high accuracy in determining pathologies. Also, a hyperspectral camera based on an acousto-optic monochromator was described in Ref. [21]. This design

eliminates the need for additional scanning systems. At the same time, the production of a control unit and shooting for a hyperspectral camera in this case turns out to be more expensive than in the device presented in this paper. Also, the used wavelength range was limited to the range of 400–750 nm, while in our study, the spectral wavelengths range is limited only by the sensitivity range of the sensor. The presented control system and an optical camera can be equipped with almost any microscope, which is almost 10 times cheaper in comparison with expensive analogs of microscopes.

4 Conclusion

The article presents a hardware and software complex for controlling hyperspectral photography, as well as software for spectral analysis. During the research, the optical characteristics of the complex were determined, software was developed for controlling the shooting and obtaining primary spatial-spectral data that are then converted into hyperspectral images by processing, which allows, as we hope, to obtain detailed and highly reliable data for establishing an accurate diagnosis from histological samples. During the study, the parameters of the shooting speed were obtained depending on the magnification of the lens.

Advantages of this complex:
1) simplicity of the scheme;
2) flexibility in the selection of specific components;
3) remote and automatic shooting control;
4) obtaining individual spectra in individual pixels of the image.

A software for spectral analysis was also developed.

Disclosures

All authors declare that there is no conflict of interests in this paper.

Acknowledgments

The development of the hardware of the hyperspectral set-top box was carried out within the framework of the state task of the Ministry of Education and Science of the Russian Federation (Project No. 0777-2020-0017), the development of the hyperspectral image analysis program was carried out with the financial support from an RSF grant No. 20-69-47110.

References

1. K. S. Tkachenko, "Application of aerospace imagery in hydrobiological research," Proceedings of the Samara Scientific Center of the Russian Academy of Sciences 14(1), 15–31 (2012) [in Russian].
2. V. S. Putilina, I. V. Galitskaya, and T. I. Yuganova, "Influence of organic substance on heavy metal migration in municipal solid waste disposal sites," Ecology. Analytical Review 76, State Public Scientific and Technical Library of the Siberian Branch of the Russian Academy of Sciences, Novosibirsk (2005) [in Russian]. ISBN: 5-94560-091-1.
3. G. Lu, B. Fei, "Medical hyperspectral imaging: a review," Journal of Biomedical Optics 19(1), 10901 (2014).
4. M. Akiko, "Hyperspectral prism-grating-prism imaging spectrograph," PhD thesis, University of Oulu (2001).
5. P. Lypaczewski, B. Rivard, G. Lesage, K. Byrne, M. D'Angelo, and R. G. Lee, "Characterization of Mineralogy in the Highland Valley Porphyry Cu District Using Hyperspectral Imaging, and Potential Applications," Minerals 10(5), 473 (2020).
6. S. Ortega, M. Halicek, H. Fabelo, G. M. Callico, and B. Fei, "Hyperspectral and multispectral imaging in digital and computational pathology: a systematic review," Biomedical Optics Express 11(6), 3195–3233 (2020).
7. I. P. Gurov, A. I. Lopatin, and A. V. Melnikov, "Formation of hyperspectral data on microscopic objects with high degree of spatial non-uniformity of optical density distribution," Scientific and Technical Journal of Information Technologies, Mechanics and Optics 2(84), 103–107 (2013) [in Russian].
8. M. M. Mazur, Yu. A. Suddenok, and V. N. Shorin, "Dual acousto-optical image monochromator with adjustable width of the hardware function," Pisma v ZhTF 40(4), 56–62 (2014) [in Russian].
9. A. G. Orlov, V. V. Egorov, A. P. Kalinin, and I. D. Rodionov, "Aviation hyperspectrometer: architecture and method of calculating elements," in 5th All-Russian Open Annual Conference on the Modern Problems of Remote Sensing of the Earth from Space, 280–287 (2007) [in Russian].
10. V. V. Podlipnov, N. A. Ivliev, and R. V. Skidanov, "A compact imaging hyperspectrometer," Journal of Physics: Conference Series 13689(2), 022053 (2019).
11. S. B. B. Ahmadi, Y. A. Nanehkaran, and S. Layazali, "Review on hyper-spectral imaging system," International Journal of Scientific and Engineering Research 4(5), 253–258 (2013).
12. J. Beach, "A richer view of bio structures," BioOptics World 2, 68–71 (2009).
13. V. Leroi, J.-P. Bibring, and M. Berthe, "MicrOmega a VIS/NIR hyperspectral microscope for in situanalysis in space," Planetary and Space Science 57(8-9), 1068–1075 (2009).
14. Raspberry Pi Documentation, Description of the operation of GPIO ports on a Raspberry Pi computer (accessed 15.07.2020) [https://www.raspberrypi.com/documentation/computers/os.html].
15. 3967 Microstepping driver with translator, Datasheets Allegro MicroSystems, Worcester, Massachusetts (2002–2003) [https://www.sparkfun.com/datasheets/Robotics/A3967.pdf].

16. Basler ace, User's manual for USB 3.0 cameras, AW001234 (2015) [https://www.micropticsl.com/wp-content/uploads/2013/09/basler_ace_usb_manual.pdf].
17. E. Myasnikov, "Evaluation of Nonlinear Dimensionality Reduction Techniques for Classification of Hyperspectral Images," In AIST (Supplement), 147–154 (2018).
18. V. I. Nozdrin, T. A. Belousova, and G. V. Trunova, "Microscopy slides for studying histology," Catalogue, Retinoids, Moscow (2016). ISBN: 978-5-93118-046-5.
19. L. A. Zherdeva, I. A. Bratchenko, O. O. Myakinin, A. A. Moryatov, S. V. Kozlov, and V. P. Zakharov, "In vivo hyperspectral imaging and differentiation of skin cancer," Proceedings of SPIE 10024, 100244G (2016).
20. I. A. Bratchenko, O. O. Myakinin, V. P. Sherendak, P. N. Volkhin, Y. A. Khristoforova, L. A. Bratchenko, D. N. Artemyev, A. A. Moryatov, O. V. Polschikova, A. S. Machikhin, V. E. Pozhar, S. V. Kozlov, and V. P. Zakharov, "In vivo hyperspectral analysis of skin hemoglobin and melanin content for neoplasia detection," Journal of Biomedical Photonics & Engineering 4(4), 040301 (2018).
21. V. Sherendak, I. A. Bratchenko, O. O. Myakinin, P. Volkhin, Yu. Khristoforova, A. A. Moryatov, A. S. Machikhin, V. E. Pozhar, S. V. Kozlov, and V. P. Zakharov, "Hyperspectral in vivo analysis of normal skin chromophores and visualization of oncological pathologies," Computer Optics 43(4), 661–670 (2019).

Characterization of Polarization Holographic Gratings Obtained on Azopolymer Thin Films by Digital Holographic Microscopy

Veronica Cazac[1,2*], Constantin Losmanschii[1], Elena Achimova[1], Alexey Meshalkin[1], Vladimir Abashkin[1], and Vladimir Podlipnov[3]

[1] Institute of Applied Physics of Moldova, 5 Academiei, Chisinau MD2028, Moldova

[2] Tampere University, Faculty of Information Technology and Communication Sciences, 1 Korkeakoulunkatu, Tampere FI-33720, Finland

[3] Samara National Research University, 34 Moskovskoye shosse, Samara 443086, Russia

*** e-mail:** veronica.cazac@tuni.fi

Abstract. Polarization diffraction gratings are formed by one-step polarization holographic recording in azopolymer thin films. The evolution of the gratings parameters, such as the modulation of diffraction efficiency and relief depth with regard to different exposure dose is analyzed. Phase-shifting digital holographic microscopy is applied for the measurement of the light-induced polarization diffraction gratings. For the accurate hologram acquisition and reconstruction of the complex amplitude transmitted by the gratings, we performed all-optical (without moving components) phase-shifting implemented within in the imaging system of the digital holographic microscope. The experimental measurement results and theoretical predictions were compared and analyzed. © 2021 Journal of Biomedical Photonics & Engineering.

Keywords: digital holographic microscopy; polarization holographic gratings; image processing; diffraction efficiency; azopolymer; thin films; phase imaging.

Paper #3433 received 25 May 2021; revised manuscript received 25 Sep 2021; accepted for publication 25 Sep 2021; published online 30 Sep 2021. doi: 10.18287/JBPE21.07.030306.

1 Introduction

Recently, azobenzene-based photochromic materials have attracted great scientific attention due to the light-induced mass migration, which can be used to create polarization holographic optical elements on thin films as a response to patterned illumination. These materials are particularly intriguing because of the reversibility of the photoinduced changes. Periodic structures created on azopolymer surfaces have many different outstanding applications such as visualizing the near-fields of plasmonic structures and the orbital angular momentum of a light beam [1, 2]. Interferometry is a flexible approach applied for the creation of complex polarization holographic gratings (PHG) with varying parameters, which would be difficult to create using conventional lithography tools. However, essential understanding and non-destructive observation of light-induced transformations in these materials is crucial and still holds great interest. PHGs represent appropriate test elements for analyzing azopolymer behavior. Digital holographic microscopy (DHM) allows you to visualize not only amplitude information, color information, but also phase information. This is especially useful for obtaining information about living cells, tissues, and various biological materials. [3–5] Digital holographic microscopy (DHM) is a quantitative phase imaging instrument [6], where complex amplitude (amplitude and phase) of light interacting with a sample are measured, by hologram acquisition. Various modifications of such microscopes are known, including a digital holographic white light microscope based on spectral phase shifting [7] DHM can also be used for 3D analysis of the profile of micro-optical components with the highest resolution [8–9].

The hologram is obtained by interference of the wave that passes through the object under study and the reference wave set under an angle in off-axis setup [10], or inline [11] in case of the phase-shifting configuration. In addition, digitalization of the interferograms open the access to the numerical processing of the complex object wavefront for revealing the phase, amplitude and 3D map of the PHG [12]. Optical and physical information about

a diffraction grating is encoded in the phase component of the digital hologram. This data permits to calculate and deduce different parameters such as the surface relief or refractive index modulation of the recorded optical elements [13–14].

In this paper, we introduce phase-shifting DHM for studying PHG recorded on azopolymer thin films. PHG were created under different recording conditions by polarization holographic recording (PHR). The analysis of the dependence of diffraction efficiency on exposure time and relief depth was carried out. The parameters of PHG obtained via phase-shifting DHM permit to extend the understanding of the light-induced topographical patterns on azomaterial surfaces.

2 Materials and Methods

2.1 Fabrication of azopolymer thin films

Carbazole-based polymer poly-n-epoxypropylcarbazole (PEPC) and azodye Solvent Yellow 3 (SY3) was applied in this study. SY3 was acquired from Sigma-Aldrich Company. The weight ratio between SY3 and PEPC was 1:3. Azopolymer was obtained by the reflux method for 8 h, from 0.33 g PEPC and 0.101 g SY3 in 10 ml toluene solution. The obtained solution of carbazole-based azopolymer (PEPC-co-SY3) was filtered. The reaction scheme is illustrated in Fig. 1. Chemical bonding of SY3 to PEPC polymer was performed by a polymerization reaction. Fabrication of the azopolymer based thin films was done via spin-coating. The main advantages of this method are uniformity and high spinning speed resulting in thin layers' deposition on a micrometer scale. The thickness of the synthesized azopolymer was 1.035 ± 0.027 μm. The measurement was carried out digitally on a modified MII-4 interferometer [15].

2.2 Recording of PHGs on azopolymer thin films

Photo-induced surface relief modulation in azopolymer thin films is closely linked to the sensibility of azobenzene compounds to the polarization of light. It was proved that the different light induced phenomena in azopolymer materials appear at a macroscopic level by a series of trans-cis-trans isomerizations cycles when their chromophores reorient perpendicularly to the electric vector of linearly polarized light [16].

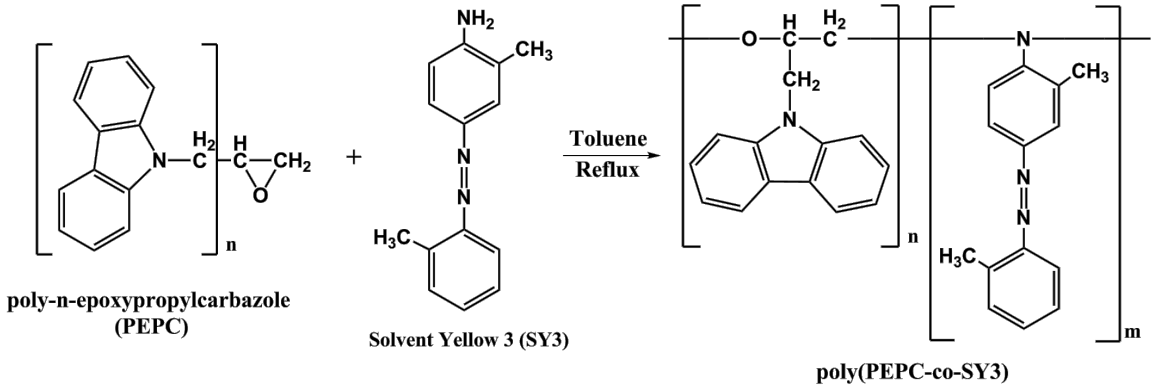


Fig. 1 Synthetic route of PEPC:SY3 azopolymer synthesis.

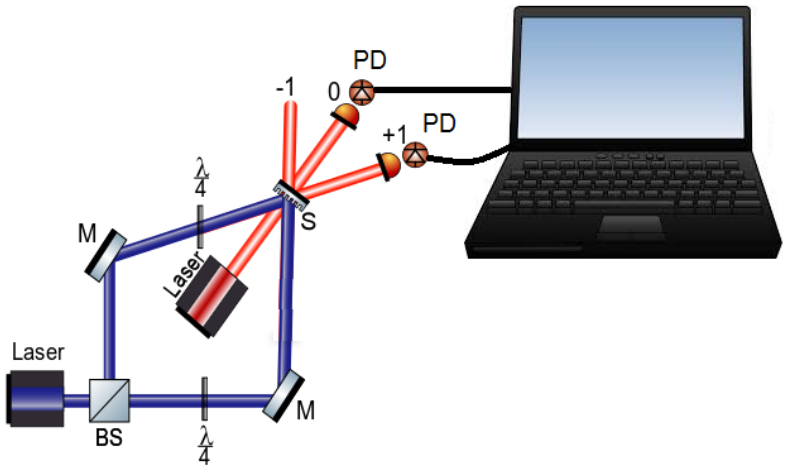


Fig. 2 Polarization holographic recording setup: laser-single mode DPSS 473 nm (100 mW), BS-polarized beam splitter, M-mirrors, λ/4-quarter wave plate, Laser 650 nm, S-azopolymer thin film, PD-photodiodes for DE registration.

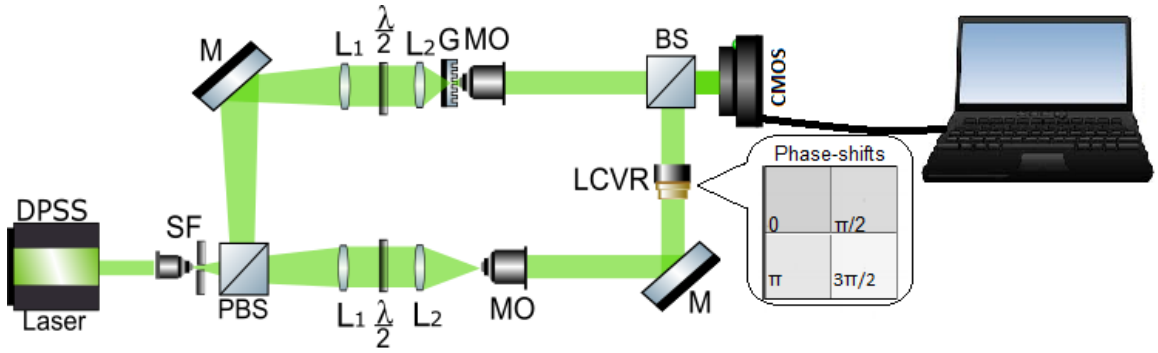


Fig. 3 The setup of the phase-shifting DHM: Laser-single mode DPSS 473 nm (100 mW), SF – spatial filter, PBS – polarized beam splitter, M-mirrors, λ/2-halve wave plate, lenses L1, L2, G-grating, MO – microobjectives, LCVR – liquid-crystal variable retarder, BS beam splitter, CMOS – digital CMOS camera.

Diffraction gratings for different exposures were made by the polarized holographic recording method. The optical setup is shown in Fig. 2. The recording laser is single mode DPSS laser (CNI Lasers MSL-FN-473), $\lambda = 473$ nm, 100 mW. The polarization of the incident beams was LCP : RCP was obtained by λ/4 wave retarders. To evaluate the performance of the obtained PHGs the diffraction efficiency (DE) evolution has been measured by two photodiodes and a red laser HLM1230, $\lambda = 650$ nm, 5 mW which does not modulate the azopolymer film. DE was determined by the following relation:

$$\eta = \frac{I_1}{2I_1 + I_0} \times 100\%, \qquad (1)$$

where, I_0 is the light intensity from zero order, and I_1 is the light intensity in first diffraction order, respectively.

Both interfering beams pass through quarter-wave plates for obtaining a polarized DOE. The angle between interfering beams is $\theta \approx 40°$ and the period of the grating on the X-axis $\Lambda = \lambda / 2\sin\frac{\theta}{2}$ is about 7 μm.

2.3 DHM investigations

The setup of the phase-shifting DHM is illustrated in Fig. 3. In the experiment, the single-mode laser beam (CNI Lasers MSL-FN-473) is divided by a polarized beam-splitter into the reference wave-R_w and the object wave that passes through the PHG- O_w. Laser beam diameters are controlled by two lenses L_1, L_2. The collimated beams pass through a half-wave plates to adapt the polarization state of the reference wave to the state of the object waves. Identical microscopic optical systems are set in both paths. The CMOS camera acquires digital holograms which represents the in-line interference pattern of beams. Four phase-shifts equal to $\varphi_1 = 0$, $\varphi_2 = \pi/2$, $\varphi_3 = \pi$, $\varphi_4 = 3\pi/2$ are produced by the LCVR (Meadowlark LVR-100 VIS), detailed calibration and explanation of the working procedures are described in Ref. [16]. The phase step is equal to π/2.

For reconstructing the map surface relief modulation of the PHGs four object holograms are captured within the grating recorded in the azopolymer film. Another four reference holograms are recorded on the area of the film that was not exposed to electromagnetic radiation. This subtraction ensures the reduction of the background noise. Finally, the phase map of the PHG is calculated by the following formula:

$$\Delta\Phi(x,y) = \Delta\Phi_0(x,y) - \Delta\Phi_R(x,y), \qquad (2)$$

where $\Delta\Phi_0(x,y)$, $\Delta\Phi_R(x,y)$ represent the reconstructed phase maps from the object and reference holograms, respectively.

3 Results and Discussions

The quality of the and surface light-induced deformations in PHGs is important for estimating the azopolymer thin films behavior under the influence of light interference. The surface relief depth (Δh) of the PHG is calculated numerically in MATLAB software from the unwrapped phase by

$$\Delta h(x,y) = \frac{\Delta\Phi(x,y)}{2\pi(n-1)}\lambda, \qquad (3)$$

where $\lambda = 532$ nm is the wavelength and n=1.6 is the refractive index of the azopolymer films.

Since refractive index modulation is small in azopolymer thin films usually, it suffices to consider only the surface relief modulation produced by modifications in the volume of the azopolymer [15]. Thus, in our calculations it is assumed that the refractive index coefficient is not changed during recording.

Theoretical calculations and experimental DHM measurement results of the PHGs obtained using differed exposure doses are illustrated in Figs. 4 and 5. The obtained gratings have a sinusoidal form. The maximal height modulation according to theoretical calculations is reached when the azopolymer is exposed for 30 min, the

value of height for this PHR is equal to 780 nm as shown by the red curve in Fig. 4. However, according to the DHM measurements the maximal modulation constitutes 650 nm corresponding to 12 min recording time.

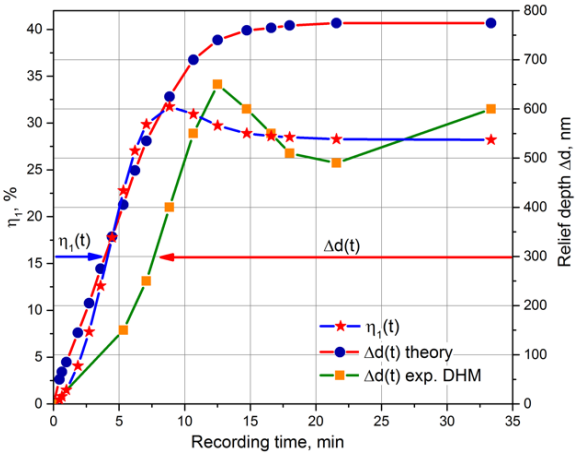
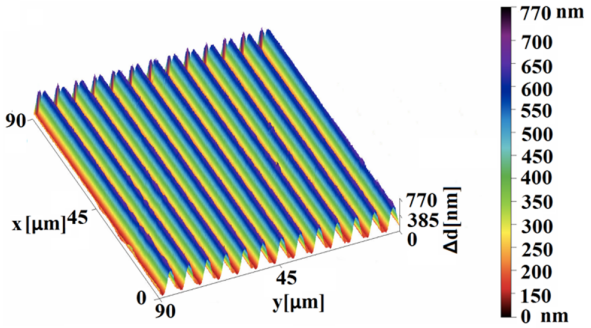
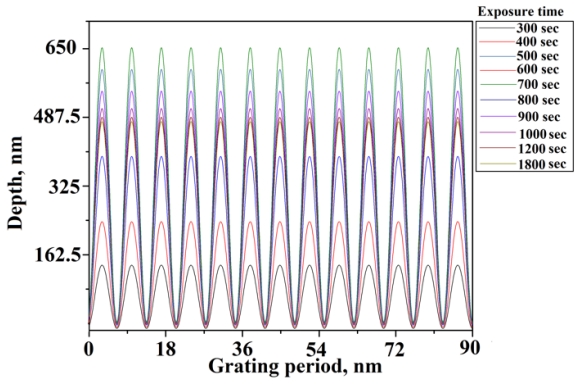


Fig. 4 Kinetics of the first-order DE of the recorded PHGs (blue), relief depth calculated theoretically (red), relief depth measured experimentally obtained by phase-shifting DHM (green).



(a)



(b)

Fig. 5 Theoretical calculations and experimental DHM measurement results of the PHGs: (a) 3D topography map of the PHG with the maximal obtained height, (b) Cross-sections taken across X-axis of the PHGs.

Discrepancies are also observed in the evolution of the relief depth. DHM measurements indicate that the height of the relief decreases after 12 min and starts to increase again after 27 min of exposure, while theoretical calculations show a constant growth, until a certain point of saturation. Remarkably, the evolution of the relief modulation defined by DHM corresponds to the kinetics of the first-order DE measured by the photo-diodes during the recording process and represented by the blue curve in Fig. 4. The kinetics reveals that maximal DE is achieved within 8 min of exposure. Fig. 5(a) illustrates the 3D topography map obtained from DHM measurements of the PHG with the maximal relief height equal to 650 nm. According to the cross-sections of the PHRs, illustrated in Fig. 5(b) the grating period is approximately 7 μm, which corresponds to the experimental recording conditions.

4 Conclusion

We have presented the procedures for micropatterning under different exposure doses of PHGs on carbazole-based azopolymers. The interferometric approach for design and characterization of the created patterns has proven to be a versatile technique. In order to realize the full potential of PHG and understand their formation dynamics and response to different exposure doses we used theoretical calculations and experimental measurements using phase-shifting DHM. The comparison between obtained experimental and theoretical parameters of the recorded PHG show particular differences in the relief depth values.

We have two assumptions on the background of this results. First, we assume that the variations in the results may be due to the refractive index changes also arising in azopolymer thin films during exposure. Second, the non-uniform modulations of the relief depth of the PHGs caused by the Gaussian beam distribution creates a difficulty to investigate the gratings in the area with maximal depth modulation [17]. Therefore, further investigations in this field would increase the knowledge on the mechanisms of photoinduced phenomena in azopolymer thin films into the phase modulation of the azopolymer thin films would further facilitate complete understanding of the behavior as well as the photonic applications of these materials, including as a sensitive medium for polarization. These materials can be useful in biomedical research. Along with the well-known methods of visualization of color, shape, and spectral properties using hyperspectral imaging microscopy [18] or Raman spectroscopy of light reflected from a micro-preparation [19], the method of digital holographic microscopy based on phase reconstruction can be extremely useful in morphological studies of micro-objects.

Disclosures

All authors declare that there is no conflict of interests in this paper.

Acknowledgments

This work was partially supported by The World Federation of Scientists National Scholarship Programme, Content NARD of Republic of Moldova BIOHOLO project 20.70086.16/COV (01.07.2020- 30.06.2021) and partially supported by "ERA.Net RUS plus" program and funded by RFBR, project number 20-52-76021.

References

1. H. Rekola, H. A. Berdin, C. Fedele, M. Virkki, and A. Priimagi, "Digital holographic microscopy for real-time observation of surface-relief grating formation on azobenzene-containing films," Scientific Reports 10(1), 19642 (2020).
2. A. Meshalkin, C. Losmanschii, A. Prisacar, E. Achimova, V. Abashkin, S. Pogrebnoi, and F. Macaev, "Carbazole-based azopolymers as media for polarization holographic recording," Advanced Physical Research 1(2), 86–98 (2019).
3. A. Anand, V. K. Chhaniwal, N. R. Patel, and B. Javidi, "Automatic Identification of Malaria-Infected RBC With Digital Holographic Microscopy Using Correlation Algorithms," IEEE Photonics Journal 4(5), 1456–1464 (2012).
4. A. S. Singh, A. Anand, R. A. Leitgeb, and B. Javidi, "Lateral shearing digital holographic imaging of small biological specimens," Optics Express 20(21), 23617–23622 (2012).
5. U. Schnars, W. Jueptner, Digital Holography: Digital hologram recording, numerical reconstruction and related techniques, Springer, Berlin, Heidelberg (2005). ISBN: 978-3-540-26911-3.
6. V. Cazac, A. Meshalkin, E. Achimova, V. Abashkin, V. Katkovnik, I. Shevkunov, D. Claus, and G. Pedrini, "Surface relief and refractive index gratings patterned in chalcogenide glasses and studied by off-axis digital holography," Applied Optics 57(3), 507–513 (2018).
7. D. Kim, J. W. You, and S. Kim, "White light on-axis digital holographic microscopy based on spectral phase shifting," Optics Express 14(1), 229–234 (2006).
8. W. Yunxin, W. Dayong, Z. Jie, L. Yan, and W. Yuhong, "3D profile measurement for micro-optical component by using digital holographic microscopy," Acta Optica Sinica 31(40), 117–122 (2011).
9. Q. Lin, D. Wang, Y. Wang, S. Guo, S. Panezai, L. Ouyang, and J. Zhao, "Super-resolution quantitative phase-contrast imaging by microsphere-based digital holographic microscopy," Optical Engineering 6(3), 034116 (2017).
10. Z. Monemhaghdoust, F. Montfort, Y. Emery, C. Depeursinge, and C. Moser, "Off-axis digital holographic camera for quantitative phase microscopy," Biomedical Optics Express 5(6), 1721 (2014).
11. M. Trusiak, J. A. Picazo-Bueno, P. Zdankowski, and V. Micó, "DarkFocus: numerical autofocusing in digital in-line holographic microscopy using variance of computational dark-field gradient," Optics and Lasers in Engineering 134, 106195 (2020).
12. V. Cazac, "Improved 3D imaging of phase shifting digital holographic microscope by compensation for wavefront distortion," Journal of Physics: Conference Series 1745(1), 012020 (2021).
13. A. Anand, I. Moon, and B. Javidi, "Automated Disease Identification With 3-D Optical Imaging: A Medical Diagnostic Tool," Proceedings of the IEEE 105(5), 924–946 (2017).
14. S. Rawat, S. Komatsu, A. Markman, A. Anand, and B. Javidi, "Compact and field-portable 3D printed shearing digital holographic microscope for automated cell identification," Applied Optics 56(9), D127–D133 (2017).
15. A. Meshalkin, A. Andries, E. Achimova, L. Bets, I. Andries, and S. Drahnea, "Interferometric Method Application for Sub-micrometers Thickness Measurements of Spin-coated PEPC and PETPC Polymer Films," in International Conference on Nanotechnologies and Biomedical Engineering, Chişinău, Republic of Moldova, 194–197 (2011).
16. A. Priimagi, A. Shevchenko, "Azopolymer-based micro- and nanopatterning for photonic applications," Journal of Polymer Science Part B: Polymer Physics 52(3), 163–182 (2014).
17. V. Cazac, E. Achimova, V. Abashkin, A. Prisacar, C. Loshmanschii, A. Meshalkin, and K. Egiazarian, "Polarization holographic recording of vortex diffractive optical elements on azopolymer thin films and 3D analysis via phase-shifting digital holographic microscopy," Optics Express 29(3), 9217–9230 (2021).
18. O. V. Polschikova, A. S. Machikhin, A. G. Ramazanova, I. A. Bratchenko, V. E. Pozhar, I. V. Danilycheva, and M. V. Danilychev, "An acousto-optic hyperspectral unit for histological study of microscopic objects," Optics and Spectroscopy 125(6), 1074–1080 (2018).
19. L. A Bratchenko, I. A. Bratchenko, A. A. Lykina, M. V. Komarova, D. N. Artemyev, O. O. Myakinin, A. A. Moryatov, I. L. Davydkin, S. V. Kozlov, and V. P. Zakharov, "Comparative study of multivariative analysis methods of blood Raman spectra classification," Journal of Raman Spectroscopy 51(2), 279–292 (2020).